Quarterly Report for

Contract DE-FG36-08GO18192

Stanford Geothermal Program

October-December 2010

Table of Contents

1. FRACTURE CHARACTERIZATION USING PRODUCTION DATA

This research project is being conducted by Research Assistant Egill Juliusson, Senior Research Engineer Kewen Li and Professor Roland Horne. The objective of this project is to investigate ways to characterize fractured geothermal reservoirs using production data.

1.1 SUMMARY

This report describes the development of a model for predicting tracer returns under variable flow rate conditions. The model is based on the one-dimensional advection dispersion equation. The model is used to define interwell connectivity and the extent to which it can be applied for fracture dominated reservoirs is explored.

The main conclusion is that if the flow paths between well pairs are strongly constrained by the fracture network, then this method works very well, and a convolution relationship exists between the injected and produced tracer concentration. The method also shows promise in cases with more complex fracture patterns. The key discovery is that the convolution is in terms of cumulative flow between each well pair (as opposed to time) and that the mixing between well-to-well flow streams can (and should) be accounted for.

The interwell connectivity is represented by a linear flow rate transformation and tracer kernel function, which can be estimated via deconvolution. Application of a nonparametric kernel estimation method is illustrated by deconvolving synthetic data generated from flow simulations. The results are verified using both cross-validation and by comparison to known solutions.

The discussion goes through examples of increasing complexity and shows how the strict application of model becomes overly cumbersome, and practically infeasible for cases where the dominant flow paths intersect far from the wells. Qualitative reasoning is given for why, for complex fracture systems, it is challenging to find a unique transfer function between well pairs from tracer return data, at variable flow rate conditions.

The final example presented is based on data from a three-dimensional fracture network, populated with 500 fractures. This example shows that, although the tracer kernels are dependent on the flow rates, they do not vary too much as to prevent reasonable predictions. Two key reasons for obtaining such reasonable results are that, much of the variability in the kernels is eliminated by taking into account; first the time delay and mixing associated with tracer transport; and secondly a transformation of time into cumulative flow.

1.2 INTRODUCTION

Understanding interwell connectivity is a requirement for geothermal field management. For example, premature thermal breakthrough can be prevented if an injector-producer pair is known to be well connected. A quantitative way of defining the connectivity leads to the possibility of optimizing reinjection scheduling (Lovekin and Horne, 1989).

Juliusson and Horne (2010) discussed a quantitative way of determining injector-producer connectivity from tracer tests. The connectivity was defined in terms of a convolution

kernel representative of the flow paths connecting each injector-producer pair. A method for estimating these kernels was developed, at steady-state flow conditions. The observation was made that the kernels do not apply for all flow rate conditions and were therefore of limited use for reinjection scheduling.

Horne and Szucs (2007) worked on characterizing interwell connectivity using tracer data collected under variable flow rate conditions. The results seemed to be promising for a field case with a highly variable flow rate history, but subsequent investigations found less success (Villacorte et al., 2010) in cases in which the flow rates did not vary sufficiently.

The methods presented in this report are extensions of those developed by Juliusson and Horne (2010). The key addition is that the convolution kernels are represented in terms of cumulative flow, and can therefore be applied at variable flow rate conditions. The mathematical basis for the method is first explained, and followed by examples that illustrate the applicability of the model.

1.3 ADVECTION – DISPERSION EQUATION FOR VARIABLE FLOW RATE CONDITIONS

Tracer returns in porous and fractured media are generally described by the advection-dispersion equation (ADE). The one-dimensional ADE can be written as:

$$R\frac{\partial C}{\partial t} = \alpha u(t)\frac{\partial^2 C}{\partial x^2} - u(t)\frac{\partial C}{\partial x} \tag{0.1}$$

where C is the concentration, x is the position, t is time, α is a characteristic dispersion length, R is the retardation factor and $u(t)$ is the time varying flow velocity. Here it is also assumed that the hydrodynamic dispersion is linearly related linearly to the flow velocity, $D(t) = \alpha u(t)$, which has been observed at various conditions in porous media (Bear 1972).

In situations where the flow rate varies it is practical to make a change of variables. Defining the following three quantities:

$$Q = A\phi\int_0^t u(\tau)d\tau \tag{0.2}$$

$$V_x = RA\phi x \tag{0.3}$$

$$V_\alpha = RA\phi\alpha \tag{0.4}$$

we can rewrite Equation (0.1) as:

$$\frac{\partial C}{\partial Q} = V_\alpha\frac{\partial^2 C}{\partial V_x^2} - \frac{\partial C}{\partial V_x} \tag{0.5}$$

The ADE is now written in terms of the cumulative flow, Q, the augmented pore volume, V_x, and the augmented dispersion volume, V_α. The volume is augmented by the factor R which represents that the tracer can adsorb to the fracture walls.

Equation (0.5) has constant coefficients and can be used in combination with the appropriate initial and boundary conditions to find standard responses in terms of Q, V_x, and V_α.

Kreft and Zuber (1978) provide a comprehensive overview of solutions to the ADE (with constant coefficients) for impulse and continuous step inputs of tracer at various boundary conditions. Kreft and Zuber emphasize that one must take note of the injection and detection modes for tracer concentration. The concentration can be measured either as the ratio of mass over fluid volume in a resident fluid, or as mass flux over fluid flux in a flowing fluid. Different boundary and initial conditions apply depending on the measurement mode.

For an impulse released into an infinite bed, that is injected and detected in a resident fluid, the initial and boundary conditions are:

$$C_r(V_x,0) = m\delta(V_x) \tag{0.6}$$

$$\lim_{V_x \to \pm\infty} C_r(V_x,Q) = 0 \tag{0.7}$$

where m is the mass injected, δ is the Dirac delta function and the subscript r refers to resident fluid measurement. The solution to Equation (0.5) using these conditions is:

$$C_{rr}(V_x,Q) = \frac{m}{\sqrt{4\pi V_\alpha Q}} \exp\left(-\frac{(Q-V_x)^2}{4V_\alpha Q}\right) \tag{0.8}$$

Here the two r subscripts refer to the injection and detection mode, respectively.

Similarly, for an impulse released into a semiinfinite bed with a flux injection (subscript f) and detection mode, the initial and boundary conditions are:

$$C_f(V_x,0) = 0 \quad for \quad x > 0 \tag{0.9}$$

$$C_r(0,Q) = m\delta(Q) \tag{0.10}$$

$$\lim_{V_x \to \infty} C_f(V_x,Q) = 0 \tag{0.11}$$

Conditions (0.9)-(0.11) lead to the flux mode solution to Equation (0.5).

$$C_{ff}(V_x,Q)=\frac{mV_x}{\sqrt{4\pi V_\alpha Q^3}}\exp\left(-\frac{(Q-V_x)^2}{4V_\alpha Q}\right) \tag{0.12}$$

Similar solutions for C_{fr} and C_{rf} can also be formulated based on the solutions given in Kreft and Zuber, although those are not stated here. The same applies for responses to continuous tracer injection.

To find the response to an arbitrary injection pattern it is useful to define the unit impulse response, or the kernel (or Green's function). From Equations (0.8) and (0.12) it is clear that the kernel would be:

$$\kappa_{rr}(V_x,Q)=\frac{1}{\sqrt{4\pi V_\alpha Q}}\exp\left(-\frac{(Q-V_x)^2}{4V_\alpha Q}\right) \tag{0.13}$$

for resident injection and detection, and:

$$\kappa_{ff}(V_x,Q)=\frac{V_x}{\sqrt{4\pi V_\alpha Q^3}}\exp\left(-\frac{(Q-V_x)^2}{4V_\alpha Q}\right) \tag{0.14}$$

for flux injection and detection.

The kernels can be used, in conjunction with the convolution theorem, to derive the response for any tracer input. The response to an arbitrary input, C_{rI}, at time zero from any location, V_x, is:

$$C_{rrP}(V_x,Q)=\int_{V_x}^{\infty}C_{rI}(V_x-\widetilde{V}_x,0)\kappa_{rr}(\widetilde{V}_x,Q)d\widetilde{V}_x \tag{0.15}$$

Similarly, an arbitrary injection of tracer from location zero over all times, $Q>0$, gives the response:

$$C_{ffP}(V_x,Q)=\int_{0}^{Q}C_{fI}(0,Q-\widetilde{Q})\kappa_{ff}(V_x,\widetilde{Q})d\widetilde{Q} \tag{0.16}$$

The subscripts *I* and *P* stand for injector and producer.

Note that when tracer flows through a sequence of one-dimensional fractures of different lengths and cross-sectional areas, the response can be computed by applying Equation (0.16) over and over again. That is, the output from the first segment, $C_{ffP,1}(V_{x,1},Q_1)$, becomes the input for the next segment, $C_{fI,2}(0,Q_2)$, which must be convolved with the appropriate kernel for segment two, in terms of the cumulative flow through that section, Q_2.

1.4 KERNEL ESTIMATION IN A SINGLE INJECTOR, SINGLE PRODUCER SYSTEM

In this section we illustrate how to obtain an estimate of the kernel, κ, that is representative of a single fracture connecting an injector and a producer. To illustrate the concept we created data using the reservoir simulator FEFLOW using variable flow rate and concentration conditions. The two-dimensional FEFLOW model, with a one-dimensional fracture, is illustrated in Figure 1.1.

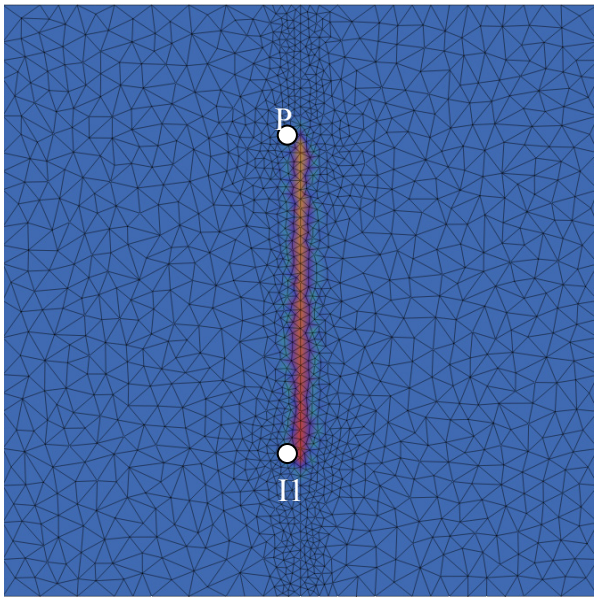

Figure 1.1: Two-dimensional FEFLOW model of tracer travelling along a single fracture. The injector and producer are labeled I1 and P1, respectively.

The injected flow rate was varied in steps as shown in Figure 1.2. Since the simulation involved single-phase liquid flow, the production rate was very similar to the injection rate.

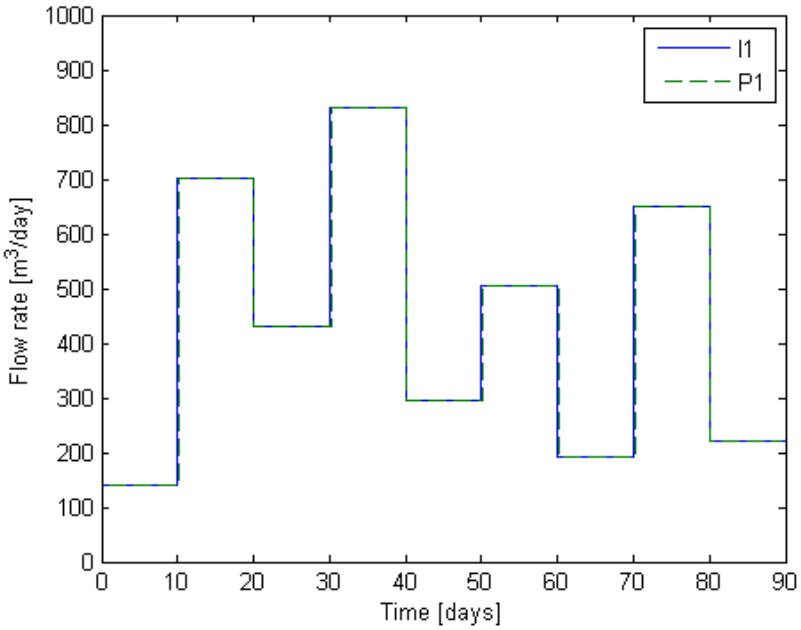

Figure 1.2: Injection and production rate for the single fracture case shown in Figure 1.1.

The injected tracer concentration was increased linearly with time, which led to the variation in produced concentration shown in Figure 1.3.

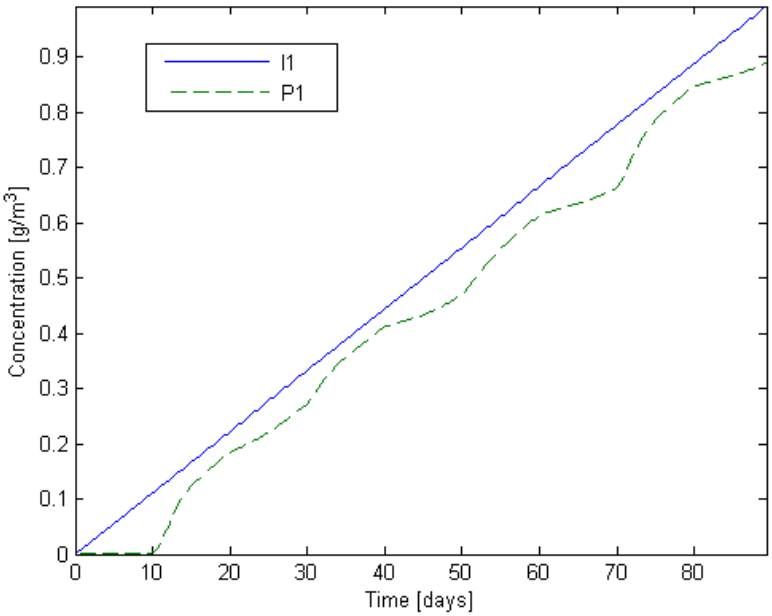

Figure 1.3: Injected and produced tracer concentration as a function of time.

To be able to find a unique mapping from the injected to the produced concentration, the variations in flow rate needed to be taken into account. This was done by viewing the concentrations as functions of the cumulative flow (we used the production rate, but the injection rate would clearly have given similar results). The injected and produced concentrations are shown in Figure 1.4, as functions of cumulative flow.

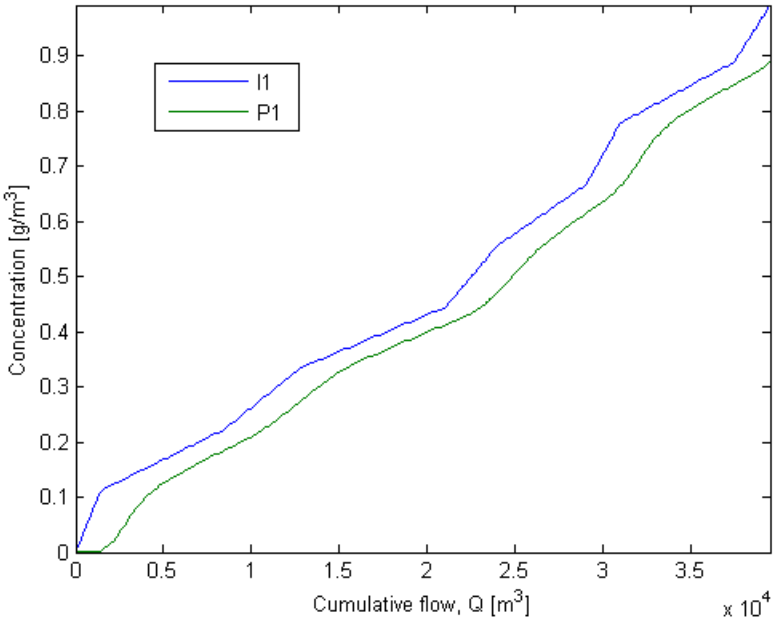

Figure 1.4: Injected and produced tracer concentration as functions of cumulative flow.

The kernel relating the two tracer concentration curves was the analog of Equation (0.14). The goal was to determine this kernel using a nonparametric deconvolution method similar to that described in Juliusson and Horne (2010).

For the production of tracer at a given point V_x the convolution integral analogous to Equation (0.16) can be approximated as:

$$\begin{aligned} C_{P1}(Q \mid V_x) &= \int_0^Q C_{I1}(Q-\tilde{Q})\kappa(\tilde{Q})d\tilde{Q} \approx C_{I1}(Q-\tilde{Q}_1)\kappa(\tilde{Q}_1)\frac{\tilde{Q}_1+\tilde{Q}_2}{2} \\ &+ \sum_{j=2}^{k} C_{I1}(Q-\tilde{Q}_j)\kappa(\tilde{Q}_j)\frac{\tilde{Q}_{j+1}+\tilde{Q}_{j-1}}{2} + C_{I1}(Q-\tilde{Q}_{k+1})\kappa(\tilde{Q}_{k+1})\left(t-\frac{\tilde{Q}_k+\tilde{Q}_{k+1}}{2}\right) \end{aligned} \tag{0.17}$$

where k was defined as $k = \left\{ j \mid \frac{\tilde{Q}_j+\tilde{Q}_{j+1}}{2} < Q \le \frac{\tilde{Q}_{j+1}+\tilde{Q}_{j+2}}{2} \right\}$. For the special case when $Q < \frac{\tilde{Q}_1+\tilde{Q}_2}{2}$ we took $C_{P1}(Q \mid V_x) \approx C_{I1}(Q-\tilde{Q}_1)\kappa(\tilde{Q}_1)Q$; and when $Q-\tilde{Q}_j < 0$ we used

$C_{I1}(Q-\widetilde{Q}_j)=C_{I1}(\widetilde{Q}_1)$. Thus, the convolution could be written as the vector-matrix multiplication:

$$\vec{C}_{P1}=\mathbf{H}\vec{\kappa} \tag{0.18}$$

where the vector $\vec{C}_{P1}$ has the same number of elements as there are data points, and $\vec{\kappa}$ has one element for each discretization point. The matrix **H** holds the time time-shifted reinjection terms, $C_{I1}(Q-\widetilde{Q}_j)$, and the interval terms, $d\widetilde{Q}$.

To determine $\vec{\kappa}$, the problem was formulated as a regularized least squares minimization problem:

$$\min_{\vec{\kappa}} \underbrace{\frac{1}{2}\left(\vec{C}_{P1}-\mathbf{H}\vec{\kappa}\right)^T\left(\vec{C}_{P1}-\mathbf{H}\vec{\kappa}\right)}_{data\ misfit}+\underbrace{\frac{1}{2}\vec{\kappa}^T R\vec{\kappa}}_{roughness\ penalty} \tag{0.19}$$

The roughness penalty (or regularization) term was formulated as:

$$\frac{1}{2}\vec{\kappa}^T R\vec{\kappa}=\sum_{i=2}^{m-1}\frac{\sigma_i}{2}\left(\kappa_{i-1}-2\kappa_i+\kappa_{i+1}\right)^2 \tag{0.20}$$

where m denotes the number of discretization points and σ_i are weighting parameters that had to be tuned to determine how much weight to place on the roughness penalty terms.

One final challenge that was faced in determining the kernel was to determine the range of the discretization terms, $\widetilde{Q}$. This was solved by using an even discretization from zero to $\widetilde{Q}_{\max}$, where the final value was found by global search algorithms (a Genetic Algorithm followed by a Pattern Search). Clearly this would not give a unique optimal value for $\widetilde{Q}_{\max}$, but it helped to focus the estimation on the transient parts of the kernel (as opposed to late time parts which were essentially zero).

The kernel representing the fracture shown in Figure 1.1 was estimated from the data shown in Figure 1.4. In Figure 1.5, the estimate is compared to an analytical solution representing the fracture.

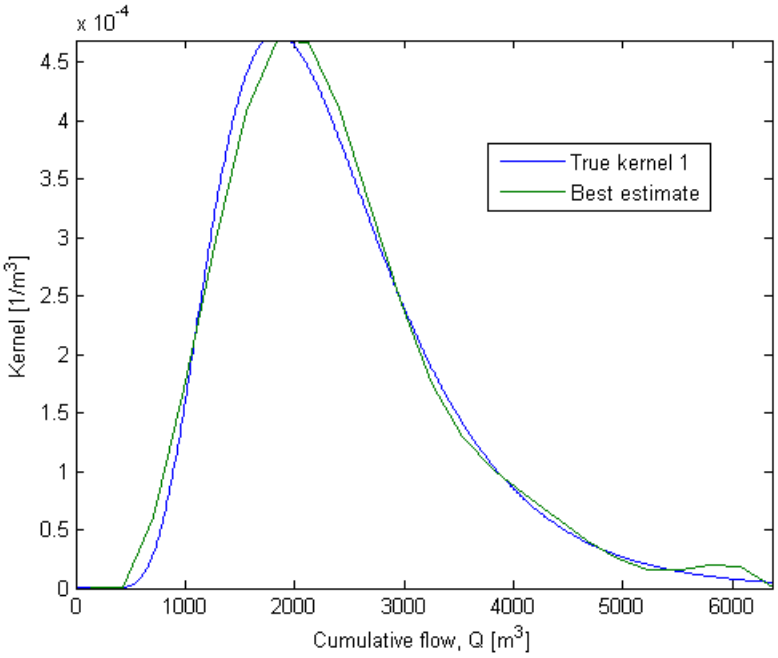

Figure 1.5: Estimation of kernel based on the deconvolution approach.

Clearly, the kernel estimate was obtained with considerable accuracy in this case, and the data misfit was very small as illustrated in Figure 1.6.

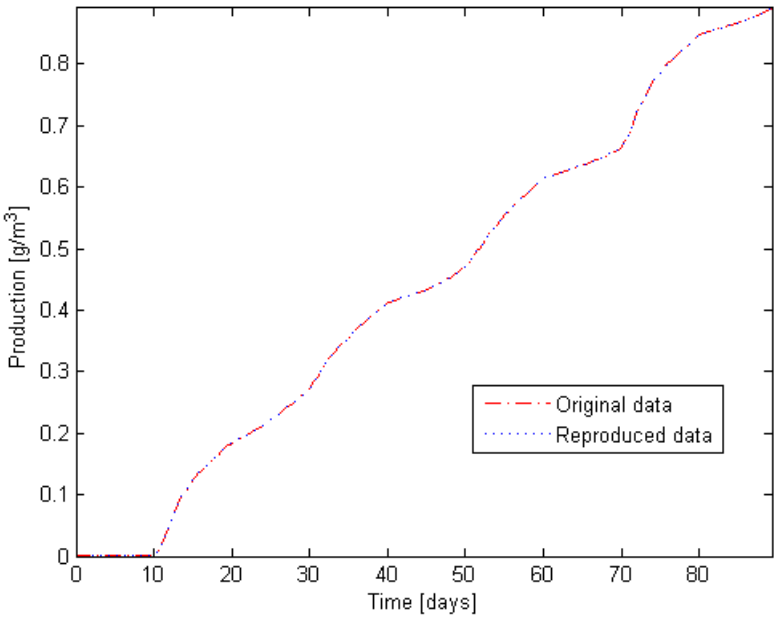

Figure 1.6: The data misfit after determining the kernel shown in Figure 1.5. The two lines are almost indistinguishable.

1.5 KERNEL ESTIMATION IN MULTIWELL SYSTEMS

In practice there are usually more than one injector and one producer, and the connectivity between each injector-producer pair is sought. Revealing these relationships based on fluctuations in production data becomes more challenging as the number of connections grows. Thus it is practical to start by analyzing a simple scenario where there are only two injectors and two producers, and no fracture intersections other than at the wells.

1.5.1 Simple Fracture Pattern

In a manner similar to that discussed in the previous section, an example flow model with discrete fractures was created (Figure 1.7). The example was set upconfigured with three fractures of equal properties in all but the fracture length, which was 60 m for the *I1-P1* and *I2-P2* fractures, but 75 m for the *I1-P2* fracture. The fractures only intersected at the wells, which was advantageous because that allowed accurate estimation of flow rates in each fracture based only on the flow rate data. This meant also that a unique kernel should be obtainable for each injector-producer combination.

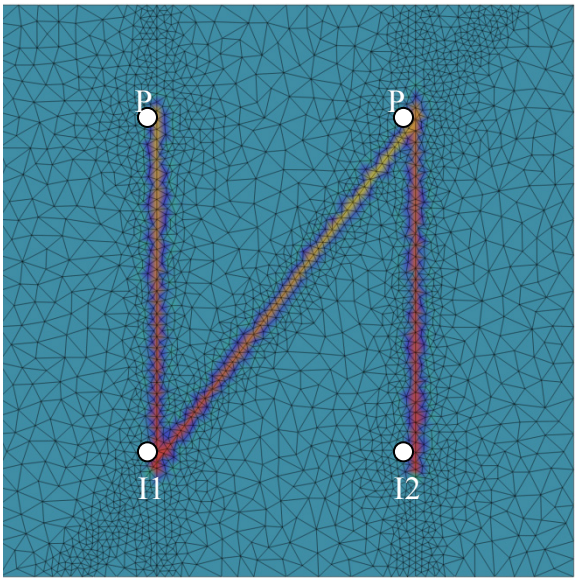

Figure 1.7: Two-dimensional FEFLOW model with two injectors and two producers. Discrete fractures connect each injector-producer pair, with the exception of I2-P1.

Flow simulations were run under variable flow rate conditions with linearly increasing concentration, as shown in Figure 1.8. At the end of 90 days, the injected tracer concentration was dropped to zero. This fluctuation was added to illustrate that the model could be used to predict large scale changes in concentration.

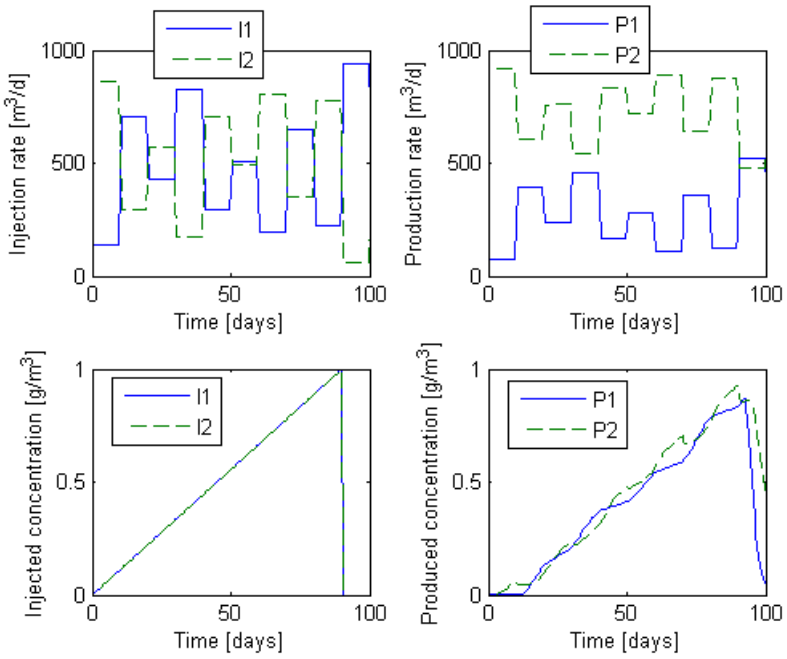

Figure 1.8: Injected and produced flow rates and concentrations for the scenario illustrated in Figure 1.7.

The single fracture model was extended to the multiple fracture case by the following formulation:

$$C_{Pj}(t) = \sum_{k=1}^{N_I} w_{jk}(t) \int_0^{Q_{jk}} C_{Ik}(Q_{jk} - \tilde{Q}_{jk}) \kappa_{jk}(\tilde{Q}_{jk}) d\tilde{Q}_{jk} \tag{0.21}$$

where N_I denotes the number of injectors and Q_{jk} refers to the cumulative flow between injector Ik and producer Pj. The weighting factor $w_{jk}(t)$ was added to account for the fact that the inflowing concentration from each injector would contribute to the concentration at Pj in proportion to the volumetric flow rate coming in. Thus, when the flow rates (q) were abruptly changed abruptly, the concentration balance would follow, albeit with a slight delay because of diffusion processes in the mixing fluids. To capture this delay we used a simple exponential kernel. Thus, the weighting factor was modeled as:

$$w_{jk}(t) = \int_0^t \frac{q_{PjIk}(t-\tau)}{q_{Pj}(t-\tau)} \frac{\exp(-\tau/T)}{T} d\tau \tag{0.22}$$

The exponential kernel was found initially by trial-and-error, but it was later seen to fit the description of a mixing cell process, with a time constant, T (Bear 1972). The flow rate q_{Pj} is the volumetric fluid production rate and q_{PjIk} is the estimated flow rate going from injector Ik to producer Pj.

A linear regression method, referred to as the MARX method (Lee et al., 2010), was used to estimate q_{PjIk}. Using this method the production rates are modeled as a linear combination of the injection and production rates at the previous time.

$$\vec{q}_P(n+1) = -\mathbf{A}\vec{q}_P(n) + \mathbf{B}\vec{q}_I(n) \tag{0.23}$$

Here n is a time like variable which was taken to represent time in increments of 0.5 days. The flow rate vectors are defined as $\vec{q}_P = [q_{P1}...q_{PN_P}]^T$ and $\vec{q}_I = [q_{I1}...q_{IN_I}]^T$. The unknowns are the elements of the matrices **A** and **B**. Compiling the observed flow rates over all n_{max} time steps gives the matrix-matrix equation:

$$[\vec{q}_P(2)...\vec{q}_P(n_{\max})] = [-\mathbf{A}\ \mathbf{B}]\begin{bmatrix}\vec{q}_P(1)...\vec{q}_P(n_{\max}-1)\\ \vec{q}_I(1)...\vec{q}_I(n_{\max}-1)\end{bmatrix} \tag{0.24}$$

Solving this equation under the constraint of $\mathbf{A} \succ 0$ (element-wise), yields the interwell connectivity matrix for flow rates:

$$\mathbf{F} = \left(\mathbf{I} + \mathbf{A}\right)^{-1}\mathbf{B} \tag{0.25}$$

This matrix relates the flow rates as follows:

$$\vec{q}_P = \mathbf{F}\vec{q}_I \tag{0.26}$$

Therefore the flow rate between each injector-producer pair was evaluated as:

$$\vec{q}_{Pj} = F_{jk}\vec{q}_{Ik} \tag{0.27}$$

The formulation given in Equation (0.21) needed to be converted to discrete form. By comparison to the single fracture case, it was clear that there would be multiple transformation matrices $\mathbf{H_{jk}}$, that were analogous to the **H** matrix for the single fracture case. The one difference was that each row was multiplied by the corresponding factor, $w_{jk}(t)$. Then, all the transformation matrices were grouped into one:

$$\mathbf{H}_j = [\mathbf{H}_{j1}...\mathbf{H}_{jN_I}] \tag{0.28}$$

Similarly the kernels referring to producer *Pj* were written as a large vector:

$$\vec{\kappa}_j = [\vec{\kappa}_{j1}...\vec{\kappa}_{jN_I}] \tag{0.29}$$

So for each producer the kernels were estimated by solving the system:

$$\min_{\vec{\kappa}_j} \underbrace{\frac{1}{2}\left(\vec{C}_{Pj} - \mathbf{H}_j\vec{\kappa}_j\right)^T\left(\vec{C}_{Pj} - \mathbf{H}_j\vec{\kappa}_j\right)}_{\text{data misfit}} + \underbrace{\frac{1}{2}\vec{\kappa}_j{}^T R_j\vec{\kappa}_j}_{\text{roughness penalty}} \tag{0.30}$$

The resulting kernel estimates, based on the first 70 days of production are shown in Figure 1.9.

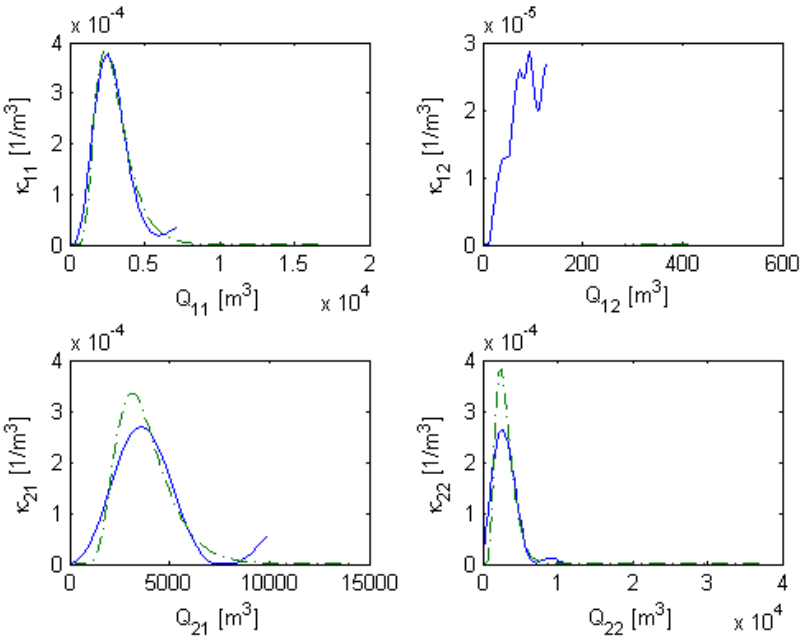

Figure 1.9: Kernel estimates for each of the injector-producer pairs. The estimates have blue solid lines, the true kernels have solid dashed lines.

The kernel for pair *I1-P1* was the most accurate since as there was very limited interference from the injection at *I2*. In contrast, the kernel for *I2-P1* was rather poorly determined, although it was determined to be very small, in terms of the magnitude of Q, making its influence negligible. This was consistent with the fact that there was no fracture connection between *I2* and *P1*. The kernels for *I1-P2* and *I2-P2* were relatively well determined. The predictive performance of the model was tested by cross-validation, i.e. using the kernel estimates to predict the concentration during the last 30 days of the production period. As shown in Figure 1.10, the variable rate kernels work well for prediction.

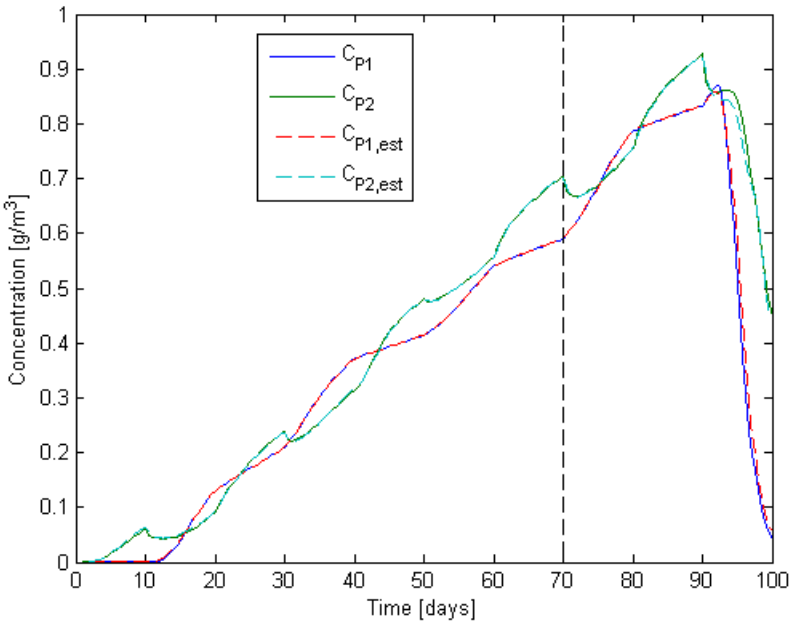

Figure 1.10: Prediction of tracer concentration in each producer, based on the kernel estimates shown in Figure 1.9. The first 70 days were used for estimation and the last 30 days were predicted.

1.5.2 More Complex Fracture Patterns

Cases of more complex fracture patterns, i.e. where the dominant flow paths would intersect in the reservoir, were considered. An example of such a fracture pattern is shown in Figure 1.11. This fracture pattern is more challenging to analyze using the kernel method because it involves six kernels (*κ1-κ6*) and three mixing cells (*m1-m3*). To be able to estimate each kernel, the flow rate in each of the six fracture segments would need to be estimated, but that cannot be done using the MARX method (nor by any other method we know of). Moreover, the signal coming through the diagonal fractures will effectively have gone through four different stages of smoothing, i.e. two kernels and two mixing cells, before it is recorded. This means that the input signal has lost a great deal of its original character and trying to back outinfer two separate kernels from such a signal seems practically impossible.

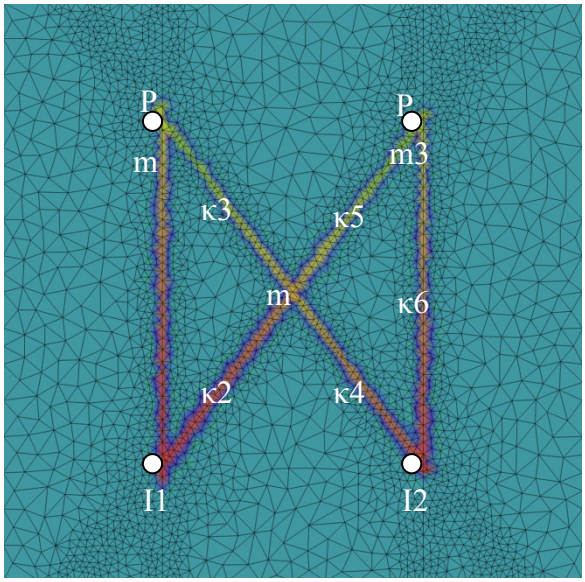

Figure 1.11: Fracture pattern with fractures intersecting in the reservoir.

Apart from the previously stated complications, we have obviously not yet begun to consider the fact that in practice one would not know the layout of the fracture network and thus how many kernels to search for in the first place. Another major complication would also arise if there were more wells in the reservoir.

Instead of considering the complex case of six kernels and three mixing cells above, one could assume that a representative kernel could be estimated for each of the injector-producer pairs. This is not rigorously correct since the kernels are functions of flow rate and the flow rates for say κ2 and κ5 will generally not be the same. However, defining the flow rate according to Equation (0.27) gave the kernel estimates shown in Figure 1.12.

The predictive power of these kernels was again verifiedexamined through by cross-validation. Data from the first 70 days were used to obtain the kernel estimates and then the concentration for the next 30 days was predicted, based on those estimates. The results are shown in Figure 1.13.

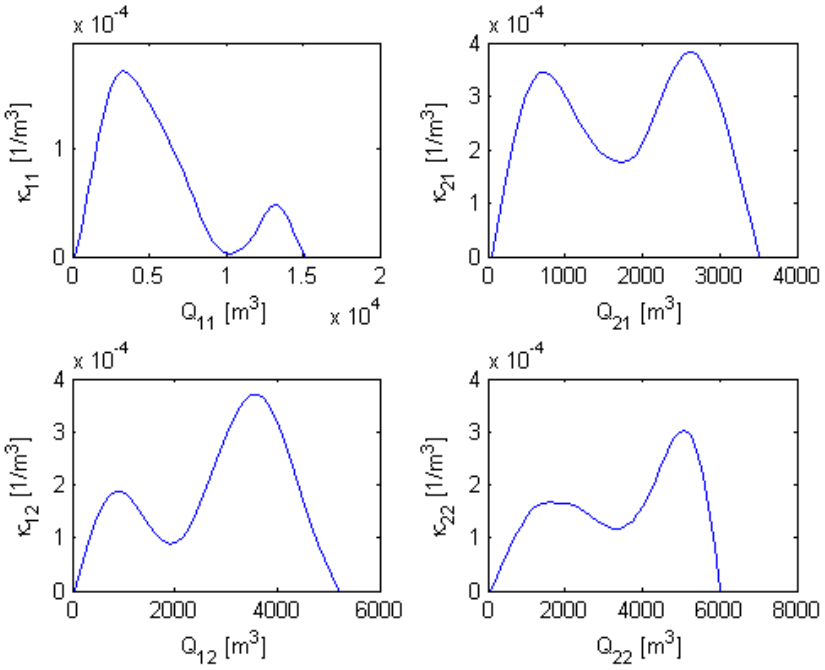

Figure 1.12: Effective kernel estimates for each injector-producer pair shown in Figure 1.11.

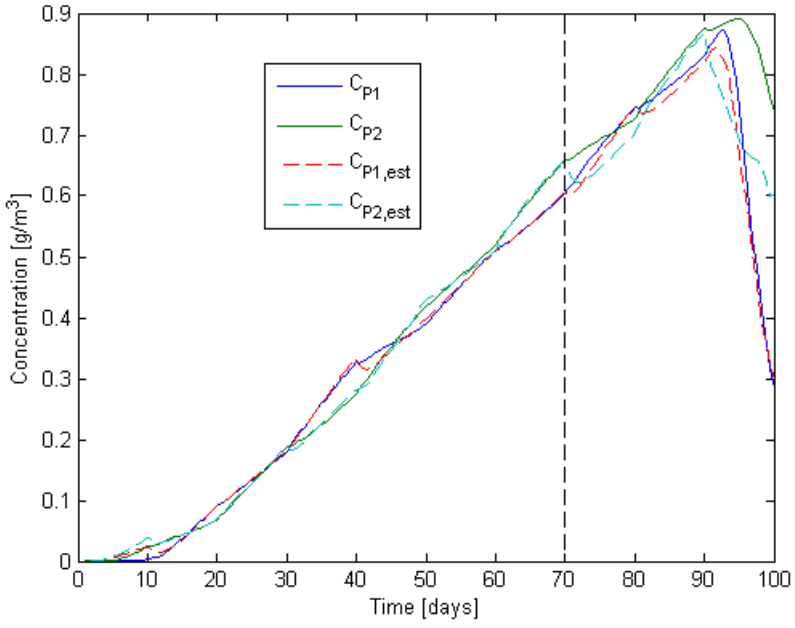

Figure 1.13 Prediction of tracer concentration in each producer, based on the kernel estimates shown in Figure 1.9. The black dashed line divides the estimation and the prediction periods.

Although the predictions in this case are not as good as those seen in Figure 1.10, they do seem reasonably accurate. This might be explained by the fact that the kernel model does capture both the fact that the injected tracer returns in a distributed manner over time, and that this time is measured in terms of the cumulative flow, which accounts for the variation in transport velocity to some extent.

As a final example, we present examined a case where a three-dimensional fracture network was created using the FRACMAN software. The fracture network had 500 fractures which were drawn from a fractal size distribution (Figure 1.14). The fracture aperture and hydraulic conductivity were correlated to the fracture size. Some qualitative analysis of the fracture network revealed that producer P2 was relatively poorly connected to the bulk of the fractures, and especially injector I1.

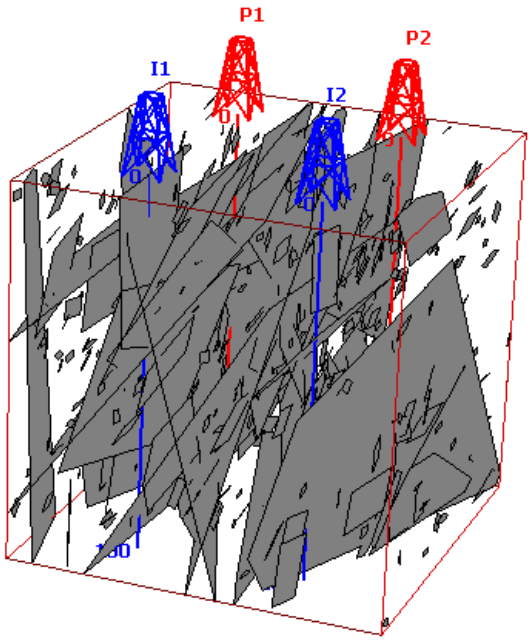

Figure 1.14: Three-dimensional fracture network generated in FRACMAN.

The fracture network was upscaled to a grid of 100 by 100 by 50 blocks, making each block 1 by 1 by 2 meters in size. The hydraulic conductivity of the blocks ranged from 10^{-5} to 12 m/s after the upscaling had been performed. Similarly the porosity ranged from 0.003 to 0.3. The upscaled data were imported into FEFLOW for flow simulation.

Four flow simulations were run, to find reference values, against which we could evaluate the kernels in this case. In each of these simulations, slugs of two different tracers were injected, one into each of the injectors. The flow rate was kept constant for the duration of each simulation, but how much was allocated to each well varied between each of the four simulations, as shown in Table 1.1.

Table 1.1: Injection rates for tracer slug simulations in the fractured reservoir shown in Figure 1.14.

	q_{I1} [m^3/day]	q_{I2} [m^3/day]
Simulation 1	200	800
Simulation 2	400	600
Simulation 3	600	400
Simulation 4	800	200

The simulated returns were normalized to account for variations in mass injected and the mixing of fluid streams, as shown by Equation **Error! Reference source not found.**(1.31).

$$\kappa_{jk}(Q_{jk}) = \frac{q_{Pj}}{q_{PjIk} F_{jk} m_{Ik}} C_{PjIk}(Q_{jk}) \tag{0.31}$$

The resulting simulated kernels are shown in Figure 1.15. The average of all four kernels is shown by the wider blue dashed line.

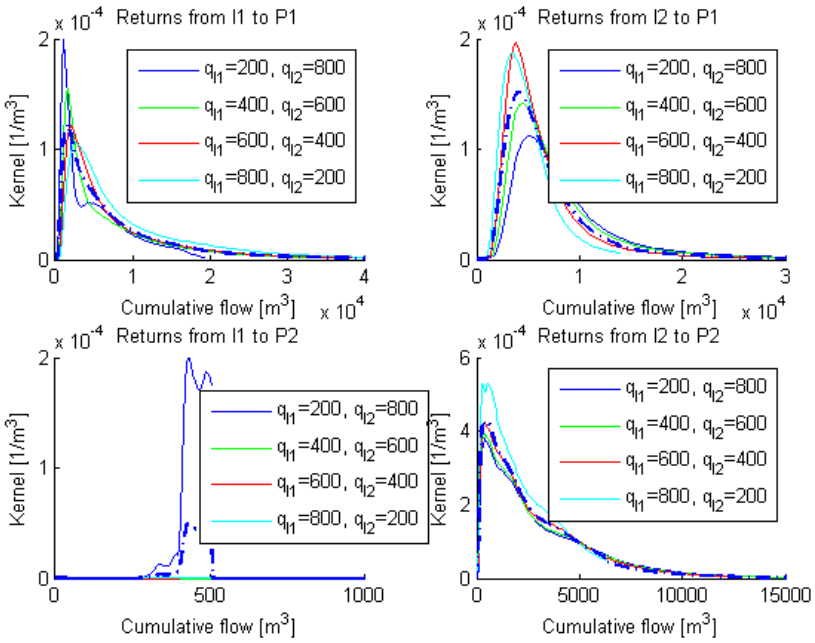

Figure 1.15: Tracer kernels as obtained from simulations of tracer tests at various flow conditions. The average of all four simulations is overlain in the blue dashed line.

Now to generate production data more similar to that found in practice, we used the injection histories shown in Figure 1.16. The simulated production rates (also in Figure 1.16) clearly show how *P1* produced considerably more than *P2*, since *P1* was connected to more of the large fractures in the reservoir. A similar observation could not as easily be made based on the tracer returns. This was because, even though a relatively small fraction

of the total tracer injected went to *P2*, most of the water produced from there came from *I2*, and the fracture connections were relatively short and small. This led to fast tracer recovery.

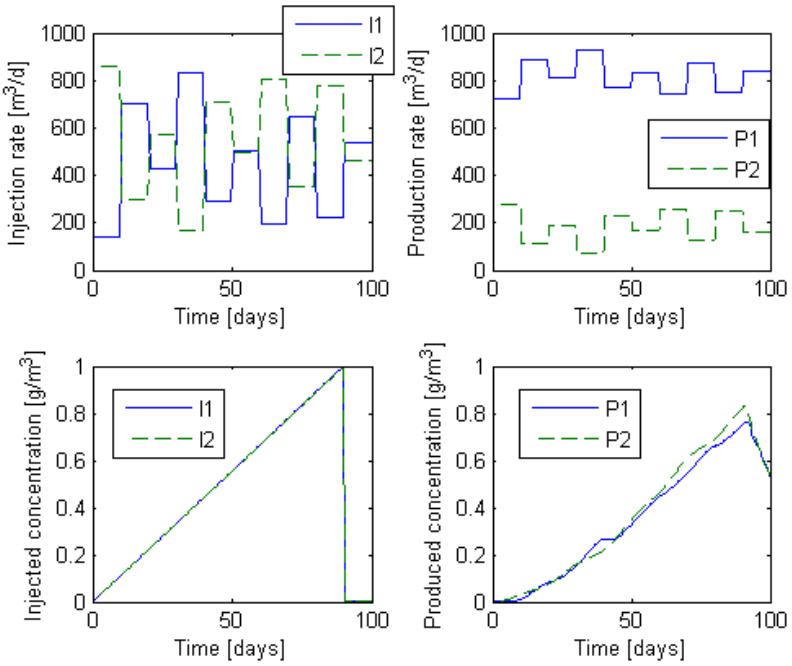

Figure 1.16: Simulated injection and production data for the three-dimensional fracture network presented in Figure 1.14.

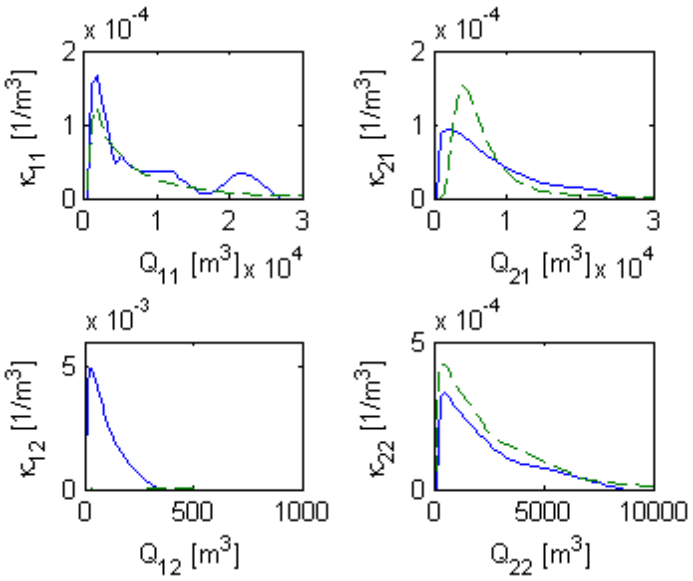

Figure 1.17: Kernel estimates obtained from production data (blue whole lines) contrasted with computed average of kernels from simulations at four different flow rate conditions (green dashed lines).

Data from the first 70 days of the simulated data set, shown in Figure 1.16, were used to estimate the kernels for each injector-producer pair. In Figure 1.17, these kernel estimates (blue whole lines) are contrasted with the average simulated kernels (green dashed lines).

The kernel estimates were finally used to predict the tracer concentration over the last thirty days. The results were quite accurate as shown in Figure 1.18.

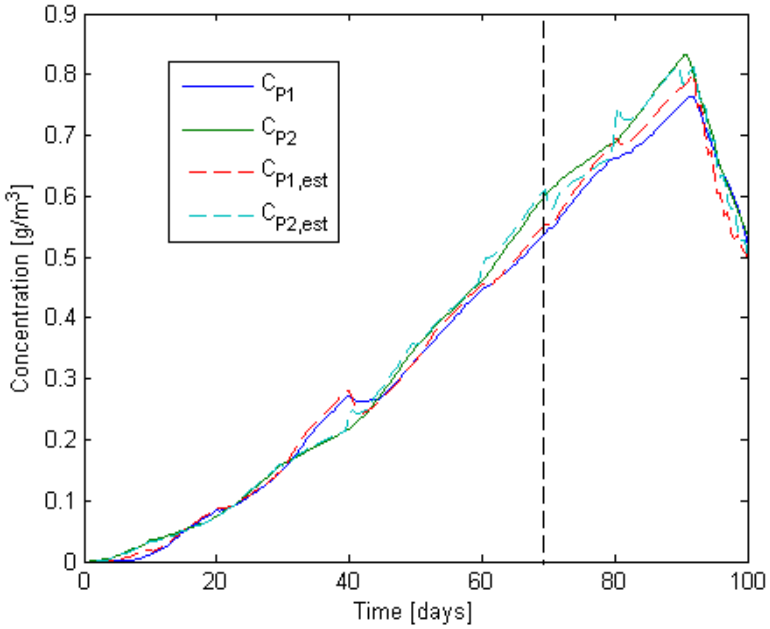

Figure 1.18: Cross-validation of tracer returns for the three-dimensional fracture network models shown in Figure 1.14. The black dashed line divides the estimation and the prediction periods.

1.6 FUTURE WORK

The predictions in the complex fracture examples were not as good as they were for the simple fracture cases. One may argue however, that the predictions were fairly close and could be useful in a practical field application. and iIt would be interesting to see how well this method performs in comparison to other known prediction methods, for example artificial neural networks or the alternating conditional expectation method. This type of analysis will be considered as an option for our future work.

A second thought is on what these results could tell us about thermal transport in the system. In this work we considered two ways of defining the interwell connectivity. One was derived from the flow rates (Eq. (0.25)), and the other was based on the tracer returns, i.e. the kernel estimates. The flow rate is governed by pressure which propagates in a predominantly diffusive manner. The tracer transport on the other hand is dominated by advective forces, i.e. forcing most of the transport through the fractures. Thermal transport is thought to occur in a mixed advective-diffusive manner through the system, and therefore the connectivity as defined by the flow rate and tracer response might give outer

bounds to the thermal connectivity. By a similar argument, a sweep-efficiency could be defined based on each of the flow rate and tracer returns, and based on that, one could narrow down the value of the thermal sweep-efficiency (or recovery factor). Further rationalization of this hypothesis will be addressed in future work.

Finally, the problem of optimizing reinjection scheduling should be revisited given this enhanced understanding of interwell connectivity.

1.7 CONCLUSIONS

A model for predicting interwell tracer returns in fractured and porous media under variable flow rate conditions was developed. A key observation was to view the tracer returns as a function of cumulative flow, as opposed to time. Each injector-producer pair was characterized by a kernel which depends on the pore volume, the dispersivity and flow capacity of the connection.

A nonparametric method for estimating the kernels was developed. The method performed very well for special cases of strongly fracture-dominated flow. For more complex fracture networks, rigorous application of the method becomes overly cumbersome, and it seems infeasible to estimate all the convolution kernels that need to be involved.

Nonetheless, reasonably good predictions were obtained by assuming that one convolution kernel could be found for each injector-producer pair. Although this method is not mathematically rigorous, it may work well in practice. The method has the advantage of capturing the delayed diffusive nature of tracer returns, and the delay is measured in terms of cumulative flow as opposed to time. Hence the method would be useful to characterize the fracture connections between wells, which is one of our primary objectives.

2. FRACTURE CHARACTERIZATION OF ENHANCED GEOTHERMAL SYSTEMS USING NANOPARTICLES

This research project is being conducted by Research Associates Mohammed Alaskar and Morgan Ames, Senior Research Engineer Kewen Li and Professor Roland Horne. The objective of this study is to develop in-situ multifunction nanosensors for the characterization of Enhanced Geothermal Systems (EGS).

2.1 SUMMARY

The injection of iron oxide (Fe_2O_3) nanoparticles coated with surfactant polyvinylpyrrolidone (PVP) was conducted to explore the nanoparticles mobility through slim tube packed with glass beads. Surfactant coating of iron oxide nanoparticles modified their surface charge. Both the nanoparticles and flow medium have negative charge. Coated iron oxide nanoparticles were identified in the effluent using scanning electron microscopy (SEM) imaging. The concentrations were determined by measuring their absorption using UV-vis spectrophotometry. The return curve showed that about 23% of injected nanoparticles were recovered.

Spherical silver nanoparticles were injected into Berea sandstone. The silver nanoparticles were identified in the effluent samples and only 25% of injected nanoparticles were recovered. Post-injection of pure water at higher injection rates and backflushing of the core sample did not result in additional recovery of the silver nanoparticles and all effluents were nanoparticles free.

Tin-bismuth nanoparticles were injected into Berea sandstone and into a tube packed with glass beads. It was found that tin-bismuth nanoparticles can be recovered following their injection into the tube packed with glass beads without being trapped within the flow conduits, but not through the pore network of the Berea sandstone. During the core injection, the tin-bismuth nanoparticles were identified in a few effluent samples at low concentrations. It was observed that smaller nanoparticles (200 nm and smaller) were transported through the pore spaces of the rock. Backflushing showed that there was entrapment of nanoparticles, including sizes greater than 200 nm. This might be attributed to an affinity of these nanoparticles to the sandstone rock matrix or high nanoparticle concentration imposing constraints to their flow. Mobility of the tin-bismuth nanoparticles in the absence of rock material was tested by their injection into the tube packed with glass beads. It was found that the tin-bismuth nanoparticles of all sizes flowed through the slim tube.

The sonochemical synthesis of tin-bismuth nanoparticles was repeated in less viscous oil in an attempt to achieve a more uniform particle size distribution, and the sample was characterized. A monodisperse sample should allow more conclusive demonstration of the size change sensing mechanism and may even aid their transport through rock. While this latest sample appears to have a narrower size distribution, the size distribution is still wider than desired.

Highlights of a review of the material science literature regarding temperature sensors are reported here. The most promising nanosensors for geothermal temperature measurement are described.

2.2 INTRODUCTION

Last quarter (July-September, 2010), experiments were carried out in which iron oxide nanoparticles coated with PVP were injected into a tube packed with glass beads. UV-visible spectroscopy and scanning electron microscopy were used to examine the effluent samples, in which no nanoparticles were detected. It was hypothesized that the concentration of coated iron oxides in the injected sample was low and may have been insufficient to be detected in the effluent, and so a more concentrated sample was prepared and the injection experiment was repeated. Spherical silver nanoparticles were also injected into Berea sandstone. The injection served as preliminary testing of the use of nanoparticles made of metal alloys (tin-bismuth), which might be used as temperature sensors in geothermal reservoirs. The silver nanoparticles were identified in the effluent samples using SEM imaging. UV-visible spectrophotometry was used to determine their concentration. It was found that about 25% of injected nanoparticles were recovered. Tin-bismuth alloy nanoparticles were synthesized and characterized, and a heating experiment was performed to demonstrate their temperature sensitivity. The results showed evidence of particle growth due to melting, but the wide size distribution made quantitative evaluation difficult.

During this quarter, we repeated the injection of iron oxide nanoparticles coated with surfactant (PVP) was into the tube packed with glass beads. The influent and effluent samples were characterized using scanning electron microscopy. The concentration of iron oxide nanoparticles in the effluent samples was measured using UV-vis spectrophotometry by measuring the nanoparticles absorption and relating it to particle concentration using a calibration curve. The return curve of the iron oxide nanoparticle production was determined. Also, we conducted a second flow experiment in which tin-bismuth nanoparticles were injected into Berea sandstone as well asinto a tube packed with glass beads. Effluent samples were fully analyzed using SEM imaging. Standard measurements on the core sample were also performed. These measurements included the liquid permeability, porosity and pore volume measurements. The tin-bismuth alloy nanoparticle synthesis was repeated in an attempt to achieve a narrow size distribution, in order to investigate their particle growth sensing mechanism more definitively. The narrower size distribution may also aid their flow through rock. Highlights of a literature review regarding temperature sensors are described.

2.3 CHARACTERIZATION OF BEREA SANDSTONE AND SLIM TUBE PACKED WITH GLASS BEAD

This section describes the measurement of the porosity, permeability and pore volume of the Berea sandstone and of the slim tube packed with glass beads.

2.3.1 Berea Core Characterization

The core sample tested during tin-bismuth injection was a Berea sandstone of 3.8 cm diameter and 5.1 cm length. The porosity and liquid permeability were determined. Porosity and permeability results are summarized in Table 2.1. The pore volume was found to be of order 10 ml. The characterization of the Berea sandstone used in the silver nanoparticle injection can be found in the last quarterly report (July-September, 2010). The porosity, permeability and pore volume were found to be 17.1% , 60.7 md and 8 ml, respectively.

Table 2.1: Porosity and permeability measurements of Berea sandstone used in tin-bismuth injection experiment.

Property	Measurement method	Value
Porosity (%)	Saturation with deionized water	17.5
Permeability (md)	Liquid permeability	125.4
Pore volume (ml)	By resaturation	10

A schematic of the apparatus used in the measurement of liquid permeability is shown in Figure 2.1.

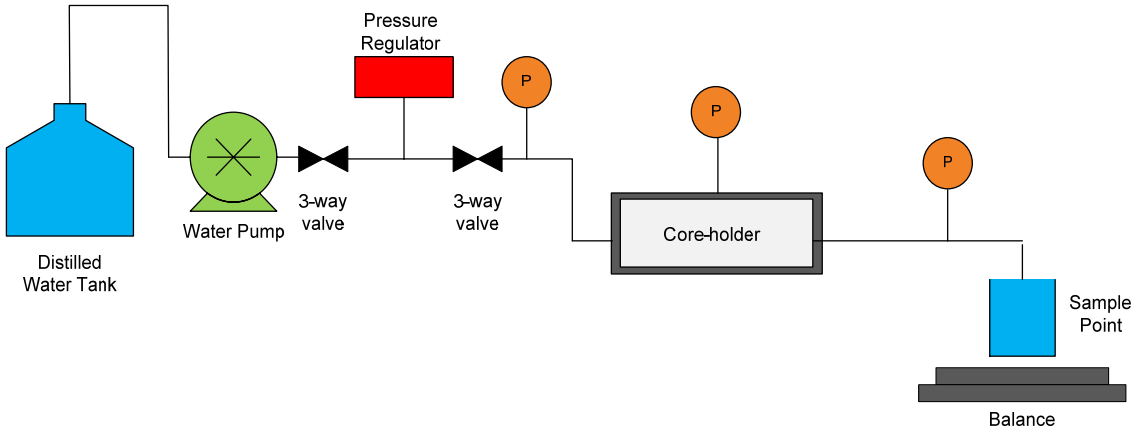

Figure 2.1: Schematic of apparatus for liquid permeability measurement.

The core sample was first saturated with water outside the core-holder. The core and related system were evacuated using a Welch Vacuum Pump for 4 hours at a vacuum pressure of about 20 millitorr to remove moisture. Pure water was introduced to submerge the sample completely. The core was then left submerged overnight and the remaining vacuum released to aid the process of saturation. After that the core was removed and wiped dry to remove excessive water on the surface. Finally, the core was weighed and hence its porosity was calculated. The core turned out to have a porosity of around 17.5 % and a pore volume of 10 cm^3. The porosity calculation is as follows:

$$\phi = \frac{V_p}{V_B} * 100 \tag{2.1}$$

$$V_p = W_s - W_d \tag{2.2}$$

$$V_B = \pi r^2 l \tag{2.3}$$

where ϕ is the porosity in percentage, V_p and V_B are pore and bulk volumes in cubic centimeter, respectively. W_s and W_d are the weight of core after and before saturation, in gram, respectively. r and l are the radius and length of the core in centimeter, respectively.

The average liquid permeability was found to be around 125.4 millidarcy. Darcy's law for horizontal flow was utilized to compute the permeability. Darcy's law for horizontal flow is given by:

$$k_{liq} = \frac{q\mu L}{A\Delta p} \tag{2.4}$$

where q is the volumetric flow rate in milliliter per second, μ is the viscosity in centipoise, L and A are the length and the cross-sectional area of the core in centimeter and square centimeter, respectively. Δp is the differential pressure across the core sample in atmospheres.

2.3.2 Polypropylene slim tube packed with glass beads

To investigate the mobility of nanoparticles in the absence of the rock materials (such as clays), iron oxides and tin-bismuth nanoparticles were injected into two separate slim tubes packed with glass beads. The 30 cm long polypropylene tubes were packed with glass beads (Glasperlen 1 mm in diameter from B. Braun Biotech International) and fitted with screens and valves at each end. A polypropylene slim tube is pictured in Figure 2.2.

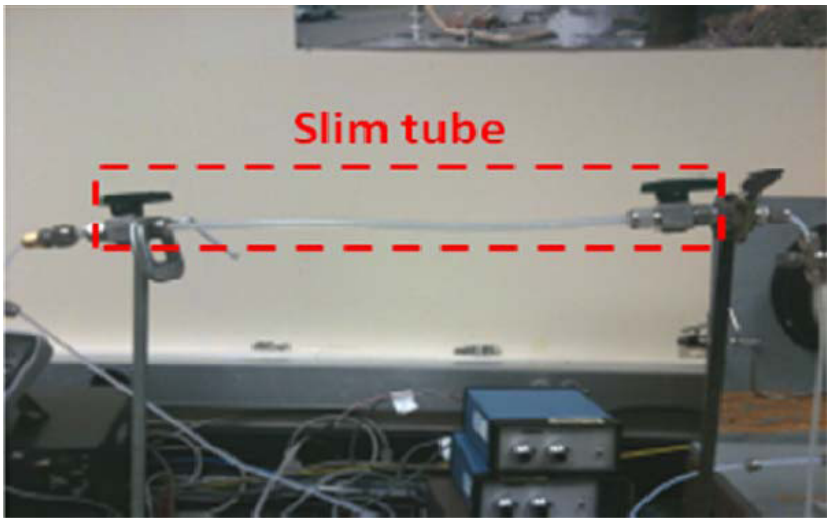

Figure 2.2: Polypropylene slim tube packed with glass beads. Two tubes were constructed: one for iron oxide and the other for tin-bismuth nanoparticle injection.

The porosity was measured by the saturation method. The porosity and pore volume of the slim tubes are summarized in Table 2.2

Table 2.2: Porosity and permeability measurements of slim tubes packed with glass beads used iron oxide and in tin-bismuth injection experiments.

Property	Iron oxide injection	Tin-bismuth injection
Porosity (%)	48	58
Permeability (darcy)	19	18.1
Pore volume (ml)	2.6	2.6

2.4 COATED IRON OXIDE CHARACTERIZATION AND INJECTION EXPERIMENT

Last quarter (July-September, 2010), iron oxide (Fe_2O_3) nanoparticles were coated with silica (SiO_2), the surfactants polyvinylpyrrolidone (PVP) and triethanolamine (TEA). The uncoated iron oxide nanoparticles exhibited very low mobility during their injection through the slim tube packed with glass beads (April-June 2010) which was attributed to their geometry and/or surface characteristics. To further investigate if the surface charge is limiting their flow, the iron oxide nanoparticles were coated with surfactants or silica to modify their surface charge. First, iron oxides coated with PVP were injected. However, they were neither detected at the effluent samples nor on the surfaces of the glass beads. Details of this injection can be found in the last quarterly report (July-September, 2010). It was speculated that the concentration of coated iron oxides in the injected sample was too low to be detected at effluent, and thus a more concentrated sample was prepared and the injection experiment was repeated.

2.4.1 Characterization of coated iron oxide (Fe_2O_3)

Coated iron oxides were characterized in terms of size, surface charge (zeta potential) and light absorption using SEM imaging, zeta potential analysis and UV-vis spectrophotometry, respectively. The original iron oxide nanoparticles were 500 nm in length and 100 nm in diameter (Figure 2.3). Surface charge measurements are summarized in Table 2.3. The reported zeta potentials are the average of three sets of measurements with standard deviation less than 1 mV.

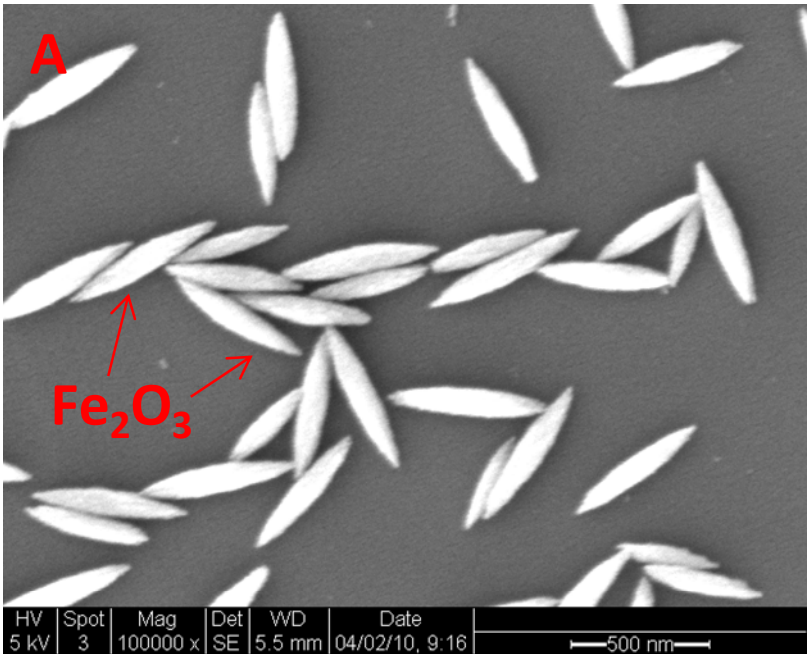

Figure 2.3: SEM image of iron oxide nanoparticles.

Table 2.3: Zeta potential and pH level for original and PVP coated iron oxide nanoparticles.

Sample	Average zeta potential (mV)	pH
Original Hematite	+59.3	3.3
Hematite-PVP	-1.06	N/A

It was evident from the surface charge measurements that the PVP coating had altered the surface charge of the original iron oxide nanorice. The original (uncoated) nanorice carries a high positive charge of 59.3 mV with low pH of 3.3 compared to the samples coated with PVP surfactant (negative 1.06 mV). The zeta potential distribution of uncoated and PVP coated iron oxide nanoparticles is depicted in Figure 2.4.

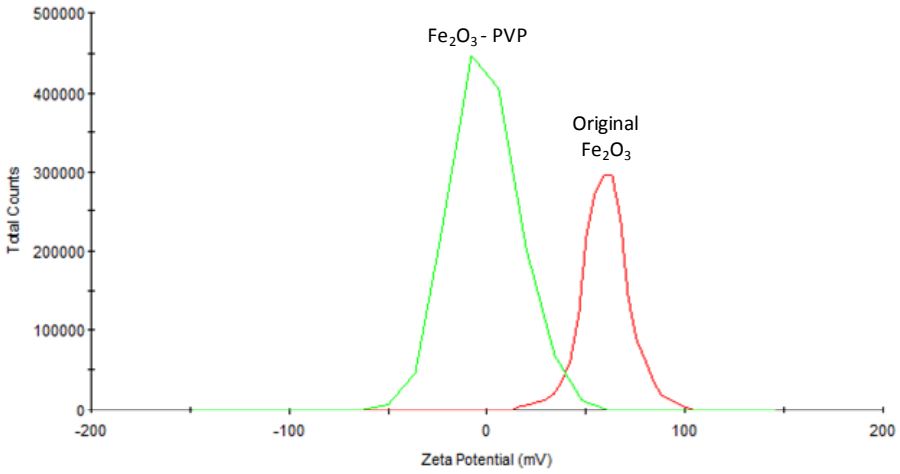

Figure 2.4: Zeta potential distribution of coated and uncoated iron oxide nanoparticles.

UV-visible spectrophotometry was used to measure the absorption of the iron oxide nanoparticles in effluent samples and hence their concentrations. This is an essential step as it enables us to construct the tracer return curve of concentrations versus volume injected. UV-visible spectrophotometry involves the spectroscopy of photons in the UV-visible region, which means that it deals with light in the visible, near-ultraviolet and near-infrared ranges. The spectrophotometer is the instrument used to measure the light intensity as a function of wavelength of light. Beer's Law is used to quantify the concentrations of absorbing species in solution (Wittung et al., 1994). The law states that the absorbance of a solution is directly proportional to the path length through the sample and the concentration of absorbing species in solution. Beer's Law is given by:

$$A = -\log_{10}\left(I / I_o\right) = \varepsilon c L \tag{2.5}$$

where A is the measured absorbance, I is the intensity of light passing through the sample, I_o is the intensity of light before it passes through the sample, L is path length through the sample, c is the concentration of absorbing species and ε is the molar absorptivity constant which is specific for each species and wavelength at particular temperature and pressure and has units of $AU / M * cm$.

Therefore, measuring the absorbance of the substance in solution and knowing the path length of the sample along with the absorptivity constant, the concentration of that substance can be calculated. Due to the difficulty in obtaining the absorptivity constant, it is common to determine the concentrations by constructing a calibration curve. By doing so, there is no need to rely on a value of the absorptivity or the reliability of Beer's Law. This is accomplished by making few dilutions, each with accurately known concentration. It is important to ensure that those concentrations bracket the unknown concentrations under investigation. For each dilution, the absorbance is measured and plotted against the sample concentration. This is the calibration curve.

The concentration of the iron oxide nanoparticles in the fluid sample was 0.25 g/cm^3. The nanofluid was diluted 1 part of nanofluid to 2, 4, 9, 17, and 35 parts of ethanol. Dilutions were made using very accurate balance and pipette. The absorbance spectra were measured at room temperature using a Shimadzu UV-1700 double beam spectrophotometer with a 12 mm square polystyrene cuvette. All samples had been sonicated prior to analysis to disperse the particles. The optical (absorbance) signatures of the diluted silver nanofluid samples are shown in Figure 2.5.

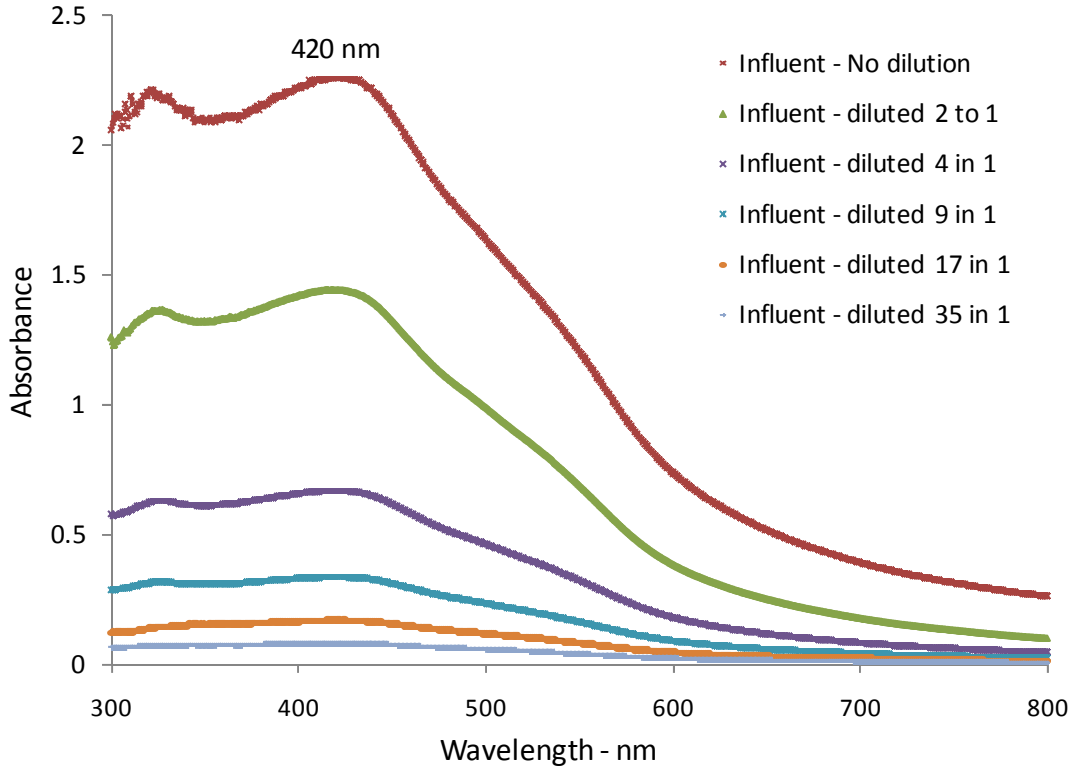

Figure 2.5: Absorbance of diluted iron oxide nanofluids of known concentrations.

The absorbance readings were all taken at a wavelength of 420 nm, as this is the wavelength at which the strongest (maximum) absorption occurs. The diluted sample concentrations and corresponding absorbance values were used to construct the calibration curve (Figure 2.6). The calibration curve was used to determine the concentration of effluent samples during the subsequent experiments.

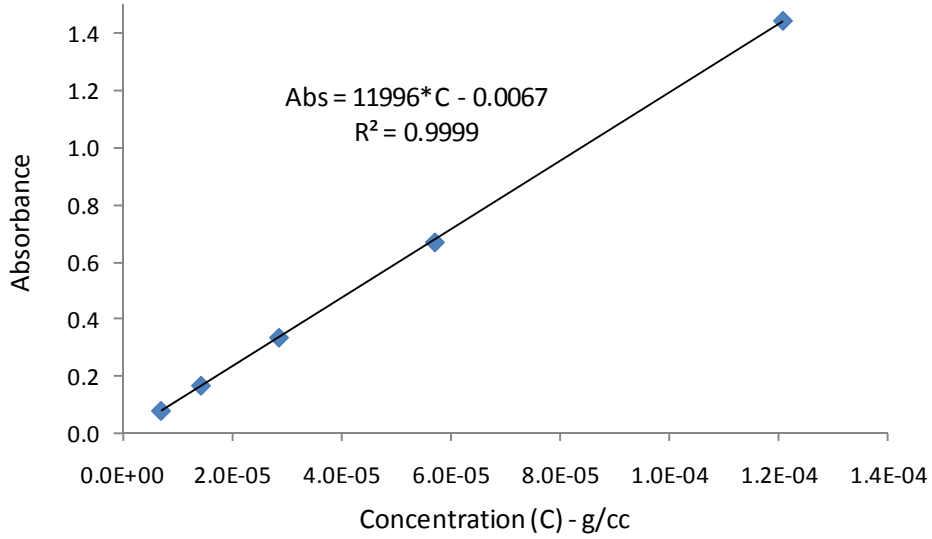

Figure 2.6: Calibration curve of iron oxide nanofluid.

2.4.2 Iron oxide (Fe_2O_3) nanoparticle coated with surfactant (PVP) injection into slim tube packed with glass beads

The iron oxide nanoparticles coated with PVP surfactant were injected into the slim tube packed with glass beads. A schematic of the apparatus used in the flow experiment is depicted in Figure 2.7.

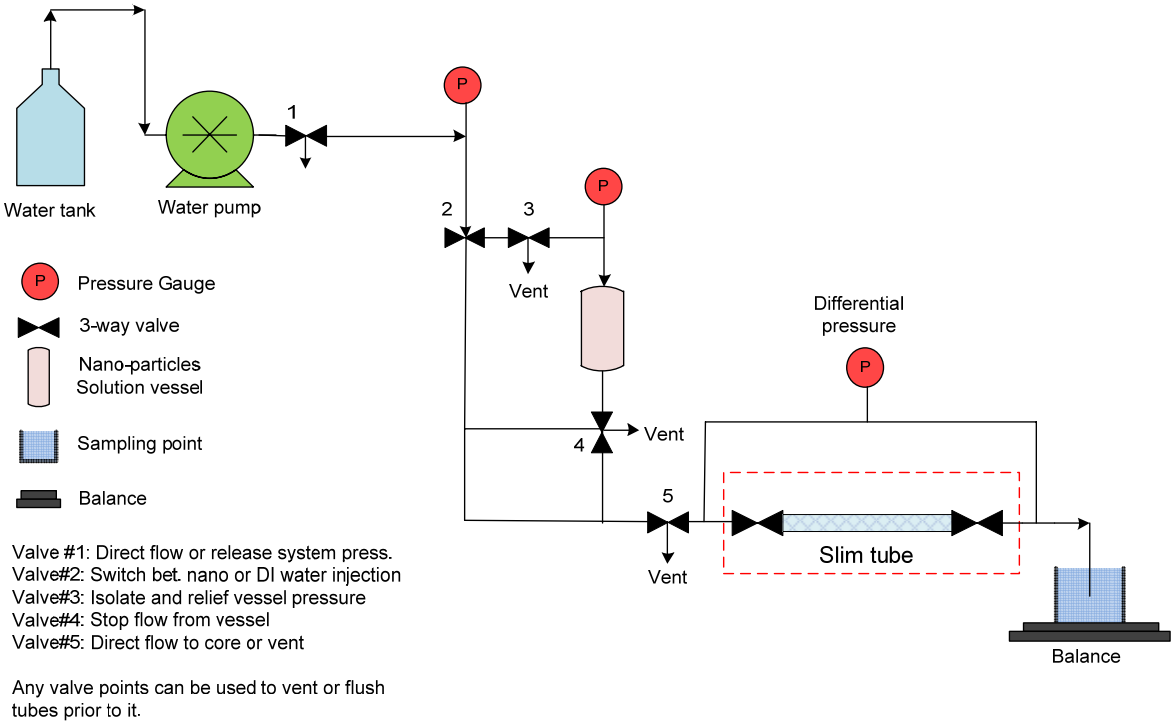

Figure 2.7: Experimental apparatus for nanofluid injection into tube packed with glass beads.

Initially, the slim tube was preflushed with several pore volumes of pure water. Then, 1 pore volume of the iron oxide nanofluid was injected at differential pressure of about 0.1 atm. Following the nanofluid injection, 14 pore volumes of pure water was injected at a rate of 0.5 ml/min and 40 effluent samples were collected. The permeability was not found to be altered during or after the injection.

2.5 SPHERICAL SILVER NANOPARTICLE CHARACTERIZATION AND INJECTION EXPERIMENT

The objective of this experiment was to investigate the transport and recovery of metal nanoparticles through the pores of Berea sandstone, initially using spherical silver nanoparticles. Initial testing began in earlier quarters with the injection of silver nanowires into Berea sandstone. The goal was to investigate the transport of a wire-like nanoparticle and determine if shape would introduce any complication to the nanoparticle flow. The silver nanowires were not detected in the effluent and were found trapped at the inlet face within the pore spaces of the core rock. The details can be found in an earlier quarterly report (July-September 2009). The injection of spherical silver nanoparticles also serves as preliminary testing of injecting spherical metal alloy (tin-bismuth) particles which might be used as temperature sensors in geothermal reservoirs.

Silver nanoparticles were characterized in terms of size, surface charge (zeta potential), light absorption and pH levels. The particle size was around 40 nm ±10 (Figure 2.8). Further details can be found in the last quarterly report (July-September, 2010).

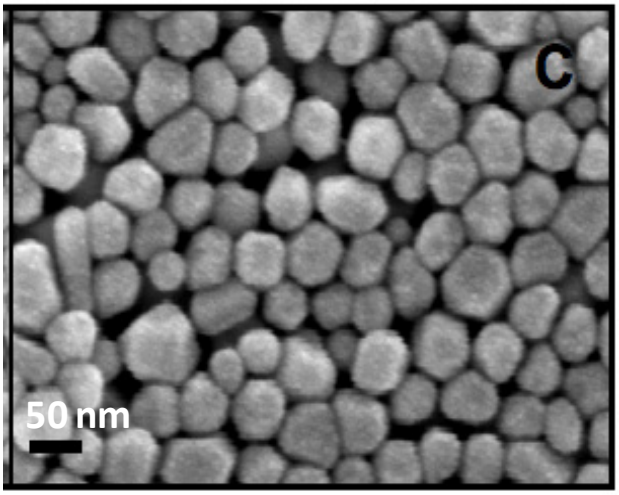

Figure 2.8 : SEM image of the silver nanoparticles.(Levard, personal communication)

Last quarter (July-September, 2010), the spherical silver nanoparticles were injected and identified in the effluent samples using SEM imaging. The concentrations were determined by measuring their absorption using UV-vis spectrophotometry. The return curve showed that less than 25% of injected nanoparticles were recovered. During this quarter, we

attempted to enhance the recovery of the sliver nanoparticles. These attempts included post-injecting pure water at higher rate and then backflushing the core rock. The flow rate of post-injected pure water was increased from 1 to 5 cm^3/min. Three pore volumes of pure water were injected. A total of nine effluent samples were collected at the rate of 2.5 cm^3 per sample. After that, the core sample was backflushed with pure water at the same injection rate and nine effluent samples were collected. The permeability was measured during all injections. Some effluent samples were selected for SEM analysis.

2.6 TIN-BISMUTH NANOPARTICLE INJECTION EXPERIMENT

Tin-bismuth alloy nanoparticles have a melting point that is tunable across a wide range of geothermal temperatures, so they have potential to be used as geothermal temperature sensors. For this reason, the transport of these particles through porous media was investigated. Nanoparticle suspensions were injected into a slim tube packed with glass beads and into a Berea sandstone core.

2.6.1 Tin-bismuth nanoparticle injection into Berea sandstone

First, tin-bismuth nanoparticles were injected into Berea sandstone. A schematic of the apparatus is shown in Figure 2.11. Nanofluid solution was contained in a pressure vessel downstream of the water pump. The tin-bismuth nanoparticles were injected with the aid of nitrogen gas. The configuration also allows for injection of particle-free water, without interrupting the flow.

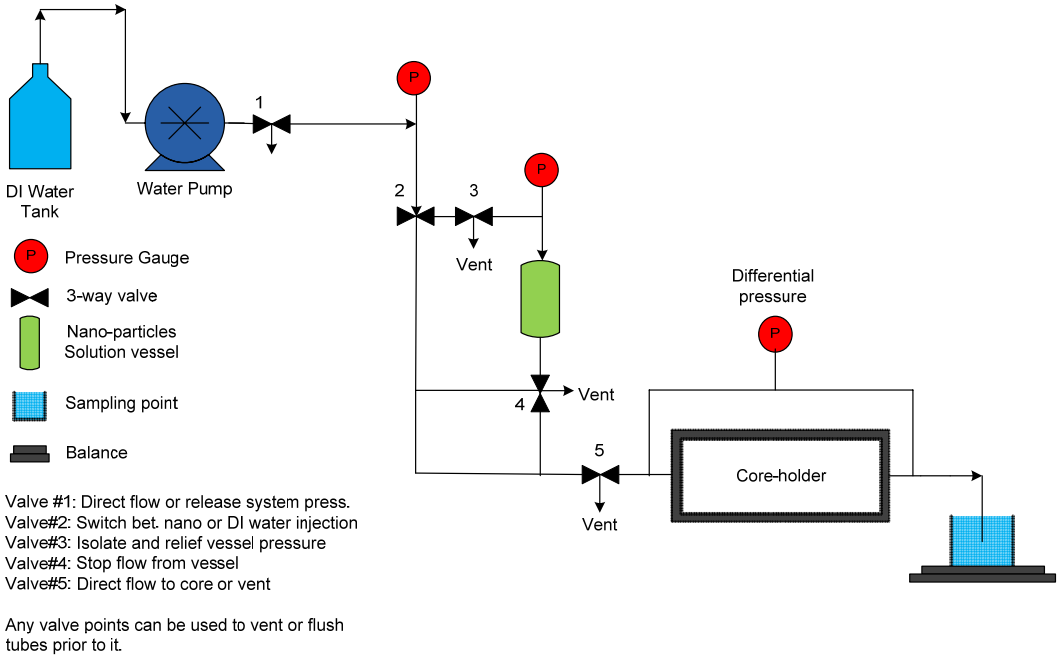

Figure 2.11: Schematic of the apparatus for tin-bismuth nanofluid injection into Berea sandstone.

Initially, the core was preflushed with pure water to displace rock fines and debris. About 30% of the pore volume (3 cm^3 of nanofluid) was then injected. Subsequent to the injection of the nanofluid, a post-injection of 13 pore volumes of pure water was

introduced. In addition, the core was backflushed with 5 pore volumes in attempt to mobilize nanoparticles that might be trapped at the inlet of the core. The injection was at the rate of 1cm^3/min. A total of 40 effluent samples were collected at the rate of 2 cm^3 per sample. The effluent sample volume was increased to 6 cm^3 for the last six pore volumes. During the backflushing of the core, the flow rate was varied between 1 to 5 cm^3/min. The higher flow rates were used to investigate their effect on the mobility of the nanoparticles. SEM imaging was used to analyze the selected effluent samples.

2.7 SYNTHESIS AND CHARACTERIZATION OF TIN-BISMUTH NANOPARTICLES

The synthesis was repeated using less viscous oil in order to obtain a narrower distribution of particle size. This would allow a more conclusive demonstration of the particle growth temperature sensing mechanism and may aid particle transport through rock.

2.7.1 Synthesis of tin-bismuth alloy nanoparticles

To perform the synthesis, Sn and Bi were melted together at the eutectic composition (~60 wt % Bi and ~40 wt % Sn). After the alloy was cooled to room temperature, two 1 g samples were sonicated in 120 ml of light paraffin oil, a slight variation of the sonochemical method suggested by Chen (2005). To investigate whether the time of sonication had any impact on the particle size distribution, Sample 1 was sonicated for 2 hours, and Sample 2 was sonicated for 4 hours. It was believed that using less viscous paraffin oil would allow more uniform energy distribution in the oil, resulting in more monodisperse particles. The VC-750 ultrasonic processor manufactured by Sonics & Materials, Inc. with a 0.75 in. diameter high gain solid probe was used. The sonicator was operated at 60% amplitude for both samples, resulting in 70.5 and 70.2 W average ultrasonic powers for Samples 1 and 2, respectively. The mixture was cooled to room temperature. The alloy particles were washed and centrifuged several times with a 1:1 mixture of hexane and acetone, rinsed in a solution of 0.1 M polyvinyl pyrrolidone (PVP) in ethanol, and finally suspended in ethanol. The centrifuge setting was 6000 rpm for 15 minutes each time.

2.7.2 Characterization of tin-bismuth alloy nanoparticles

The tin-bismuth alloy nanoparticles were characterized in terms of size and shape using SEM imaging (Figures 2.12 – 2.15).

Visually, it was estimated from Figures 2.12 – 2.15 that the particles are predominantly spherical with sizes range from about 50 nm to larger than 500 nm. It seems that the particle size distribution resulting from using less viscous oil may be somewhat narrower than the previous synthesis, but the distribution is still too wide. It can also be inferred that sonication time had little impact on the particle size distribution. It is therefore hypothesized that using a high sonication power is the best route to obtaining the

monodisperse particles reported by Chen et al. (2006). Particle size separation by centrifugation is another possible route.

Particle aggregation was observed in Figures 2.12 – 2.15, which may be attributed to aggregation on the substrate. The particles also have a blackberry-like texture (most visible in Figure 2.15). This may be attributed to the smaller particles aggregating onto the surface of larger ones in order to reduce their surface energy.

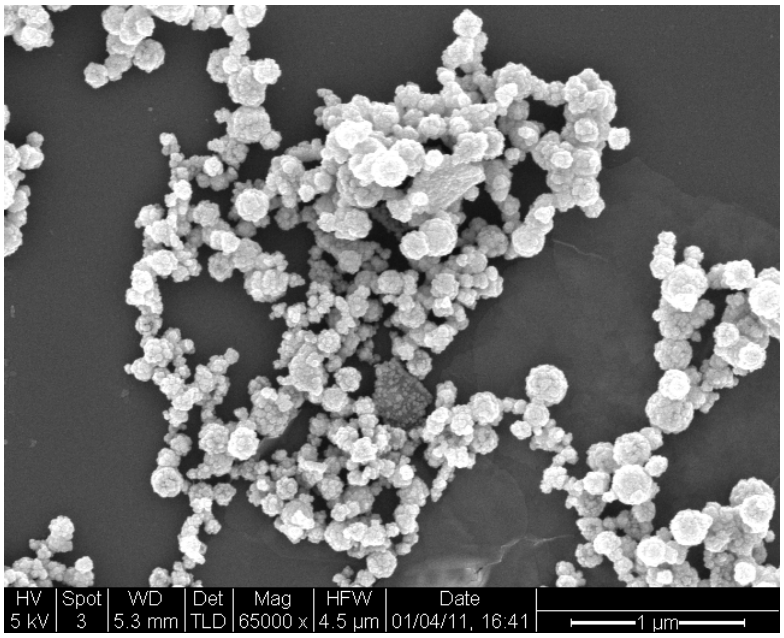

Figure 2.12: SEM image of Sample 1 at 65,000× magnification.

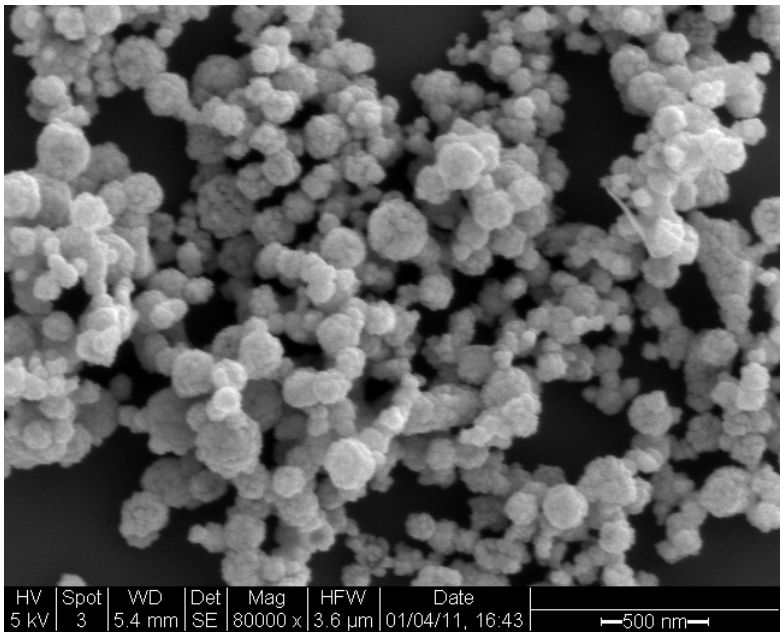

Figure 2.13: SEM image of Sample 1 at 80,000× magnification.

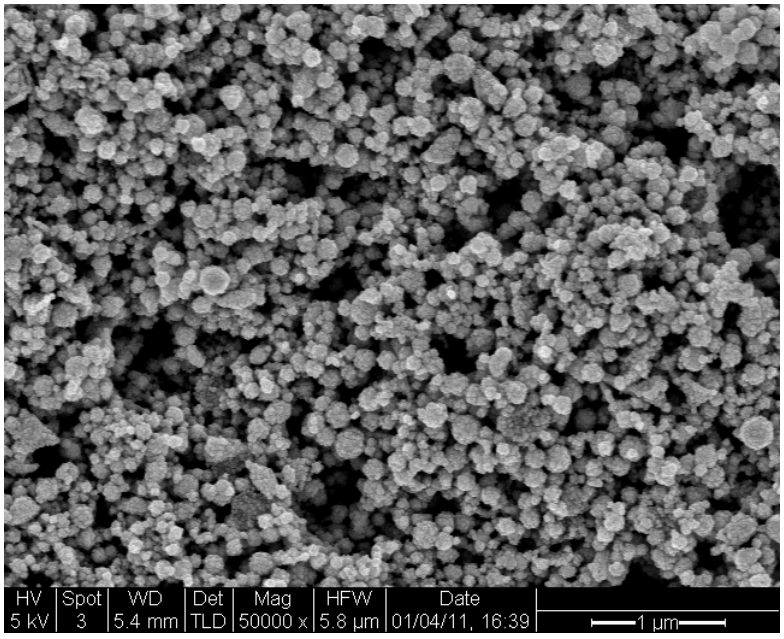

Figure 2.14: SEM image of Sample 2 at 50,000× magnification.

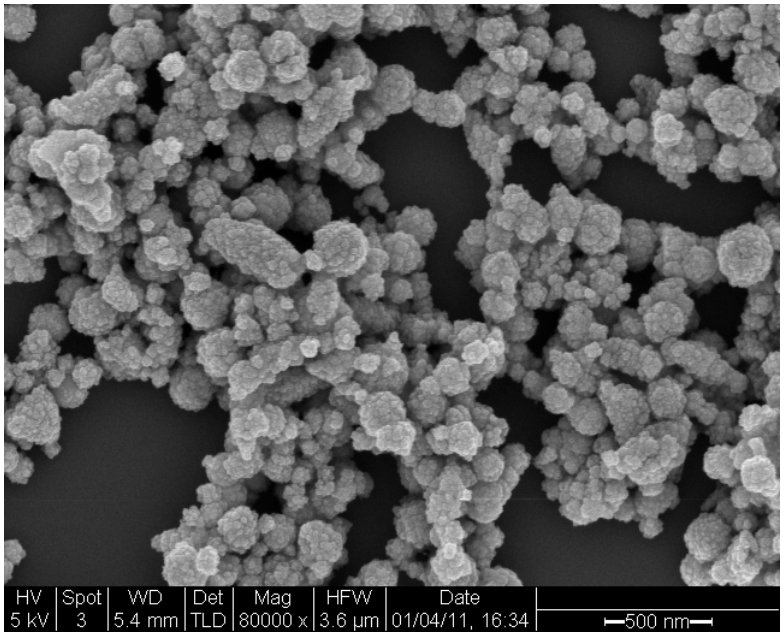

Figure 2.15: SEM image of Sample 2 at 80,000× magnification.

2.8 RESULTS

During this quarter, two main flow experiments were conducted; the injection of iron oxide nanoparticles coated with surfactant (PVP) into a tube packed glass beads, and the injection of tin-bismuth nanoparticles into a Berea sandstone and into a tube packed with glass beads. Backflushing, injecting at higher flow rates and brine post-injection into Berea

sandstone used earlier in the silver nanoparticle injection experiment were also performed. Finally, the synthesis of tin-bismuth nanoparticles was repeated in order to achieve a narrower particle size distribution.

2.8.1 Iron oxide coated with surfactant (PVP) injection experiment results

To determine whether the transport of iron oxide nanoparticles was limited by their surface characteristics, iron oxide was coated with SiO_2 and the surfactants TEA and PVP to modify its surface properties. Among these three, iron oxide coated with PVP was selected for injection (July-September, 2010). The iron oxide nanoparticles were transported through the tube packed with glass beads and were detected in the effluents. SEM imaging confirmed the transport of the nanoparticles as shown in Figure 2.16.

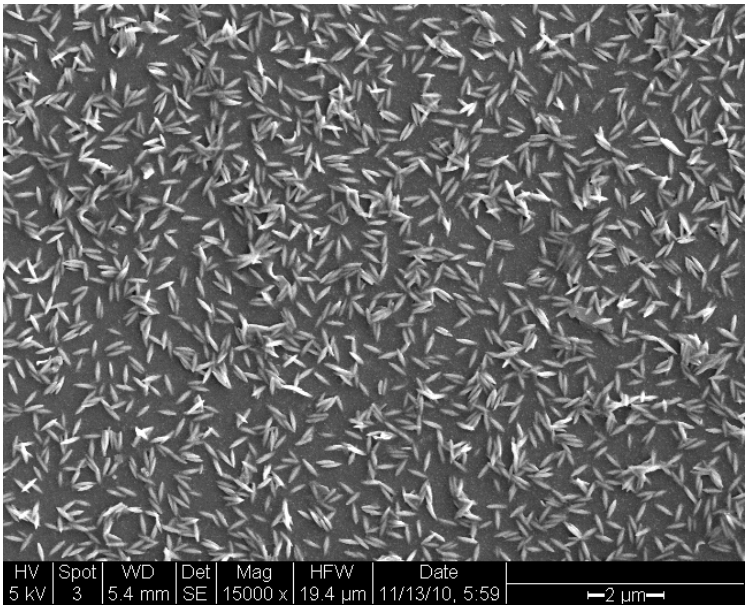

Figure 2.16: SEM image of effluent sample taken from the third post-injected pore volume.

The recovery of the iron oxide nanoparticles was also confirmed by dynamic light scattering (DLS). The size reported by DLS was the average size obtained when the light struck the particles from different angles. These iron oxide nanoparticles were 500 nm in the longitudinal direction and 100 nm in traverse direction. During the measurement, the light hits the nanoparticles from all directions and the reported size is an average size between 100 to 500 nm, depending of the sample concentration. Figure 2.17 shows the dependency of the nonspherical nanoparticle size measurements on sample concentration. Several dilutions of iron oxide nanofluid were prepared and DLS measurements were performed. The average size of the nanoparticles represented by the peak of the distribution changed with any change in sample concentration. There was a shift of about 300 nm of the peak of the distribution between the original and the most diluted nanofluid sample. DLS measurements performed on effluent samples at the fourth and fifth post-injected pore volumes were found to match the size distribution of dilutions (1 to 32) and (1 to 256), respectively (Figures 2.18 and 2.19)

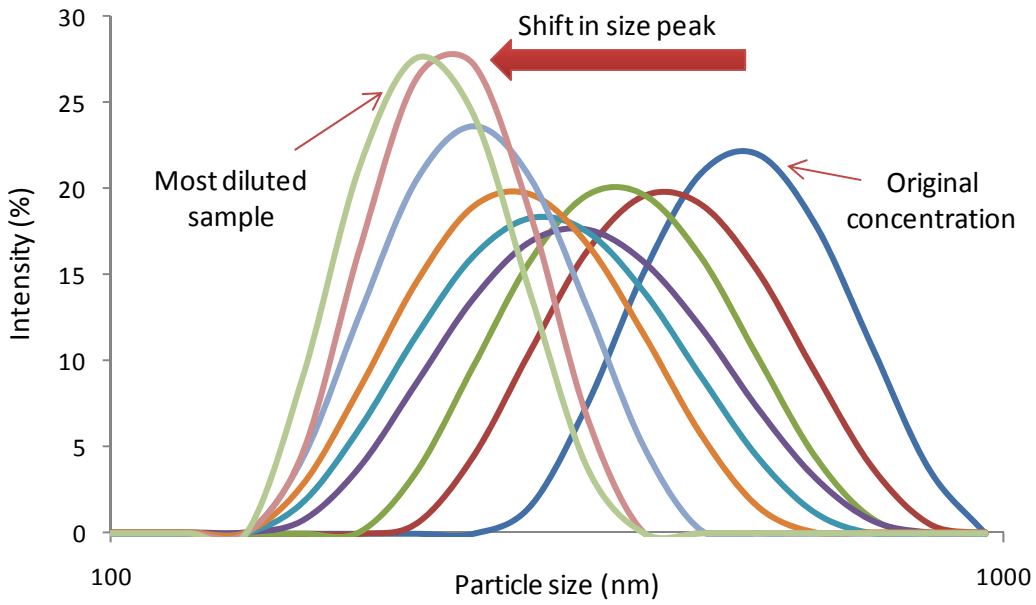

Figure 2.17: DLS measurements of size distribution of iron oxide nanofluids at various concentrations. The graph shows the shift in the peak of the distribution as concentration changes.

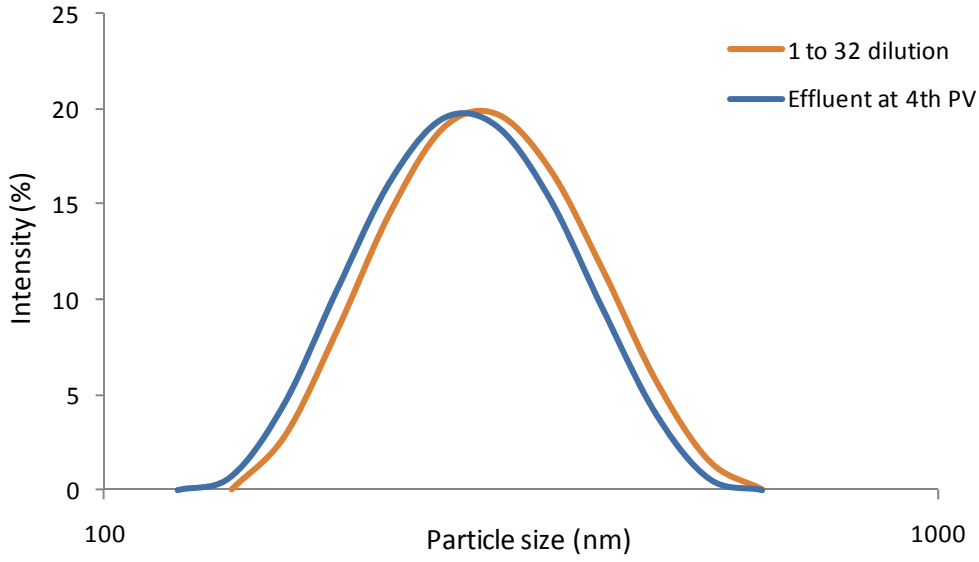

Figure 2.18: Size distribution of effluent sample at the fourth post-injected pore volume. This matches the size distribution of a diluted sample.

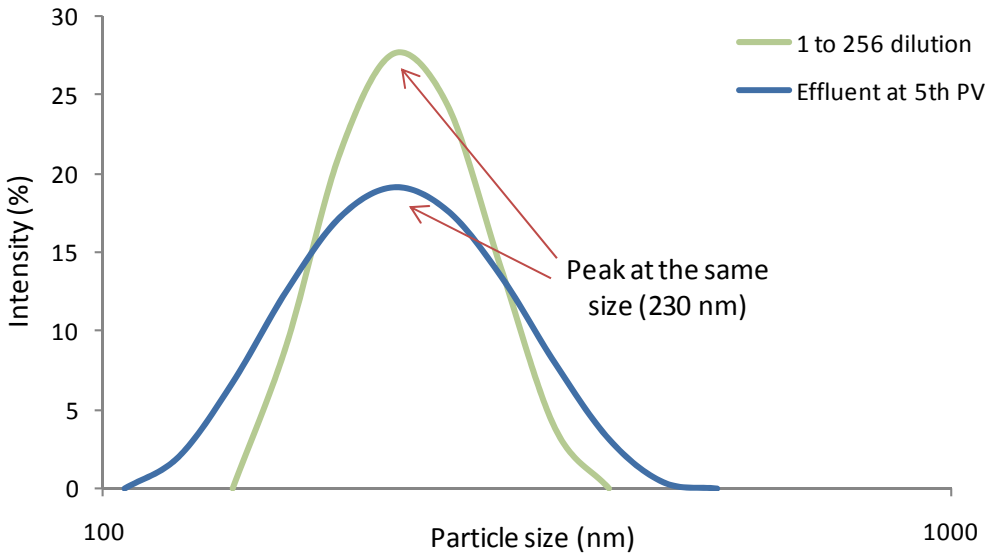

Figure 2.19: Size distribution of effluent sample at the fifth post-injected pore volume. This matches the size distribution of a diluted sample.

The concentration of the effluent samples was determined by measuring their absorbance using the UV-vis spectrophotometry. The absorption spectra for all effluent samples are depicted in Figure 2.20.

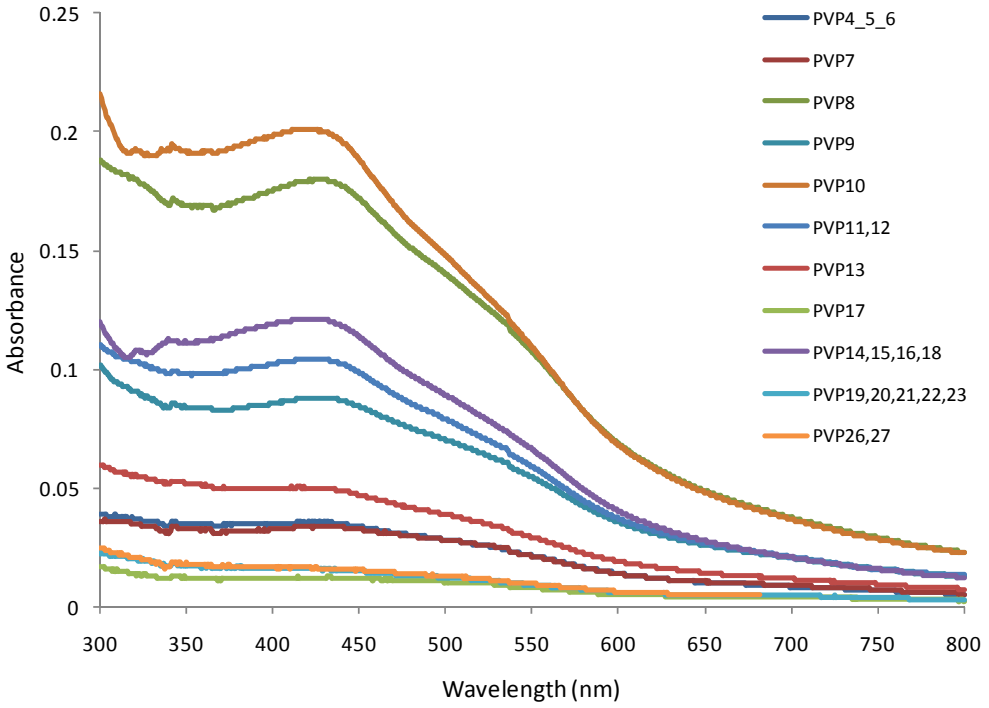

Figure 2.20: Absorbance of all effluent samples collected during iron oxide nanoparticles injection experiment.

Most absorbance spectra had identical signature. The absorbance spectra of samples PVP 4, 5 and 6 could not be measured separately, perhaps due to their low concentration, and thus they were mixed together and one absorbance spectrum was obtained. The same approach was applied to samples PVP 11-12, PVP 14-18, PVP 19-23 and PVP 26-27 at the third, fourth, fifth and sixth post-injected pore volumes, respectively. Dilution was carried out wherever required.

The calibration curve was then used to obtain the corresponding concentrations for all samples. Diluted sample concentrations were calculated using the following linear relationship.

$$C_1V_1 = C_2V_2 \tag{2.6}$$

where C_1 and C_2 are concentrations before and after dilution, respectively. V_1 and V_2 are sample volumes before and after dilutions, respectively.

Following the determination of the effluent samples concentration, the production history curve of the iron oxide nanoparticles coated with PVP was estimated (Figure 2.21).

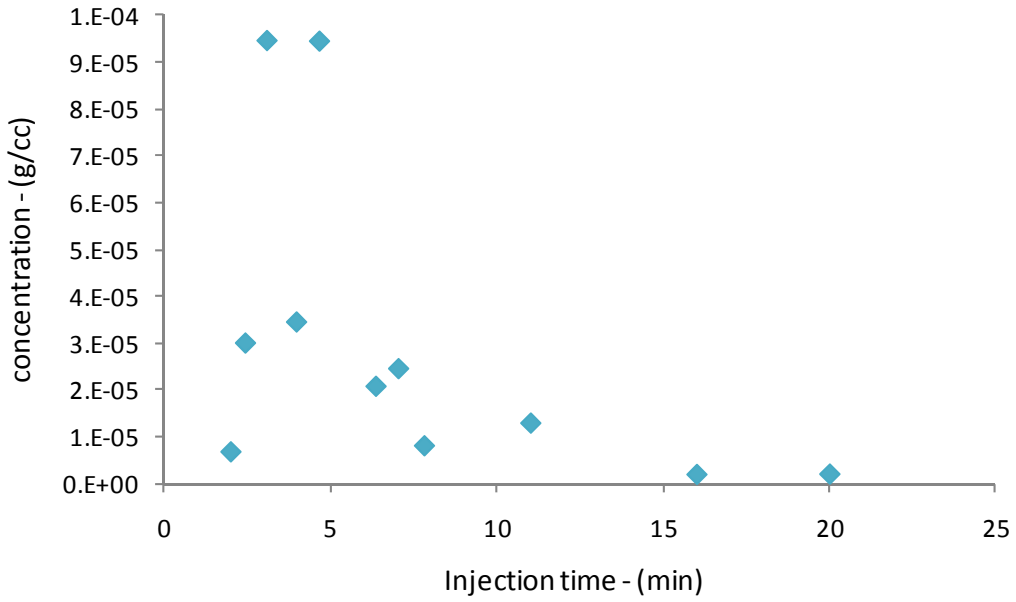

Figure 2.21: Production history (return curve) of coated iron oxide nanoparticles surfactant (PVP).

The number of nanoparticles recovered can be calculated by integrating the area under the return curve. A rough estimate has indicated that less than 23% of injected nanoparticles were recovered.

2.8.2 Spherical silver nanoparticles injection experiment results

Spherical silver nanoparticles were detected in the effluent samples and about 25% of injected nanoparticles were recovered as reported in last quarterly report (July-September, 2010). This quarter, post-injection of pure water was performed at higher flow rate to investigate if larger flow rates would improve the recovery. The rock was also backflushed at the same rate in an attempt to mobilize nanoparticles trapped at the inlet of the core. The silver nanoparticles were not detected in any of the effluent samples collected during high flow rate injection or backflushing. During backflushing, the permeability was improved by about 25 md as depicted in Figure 2.22.

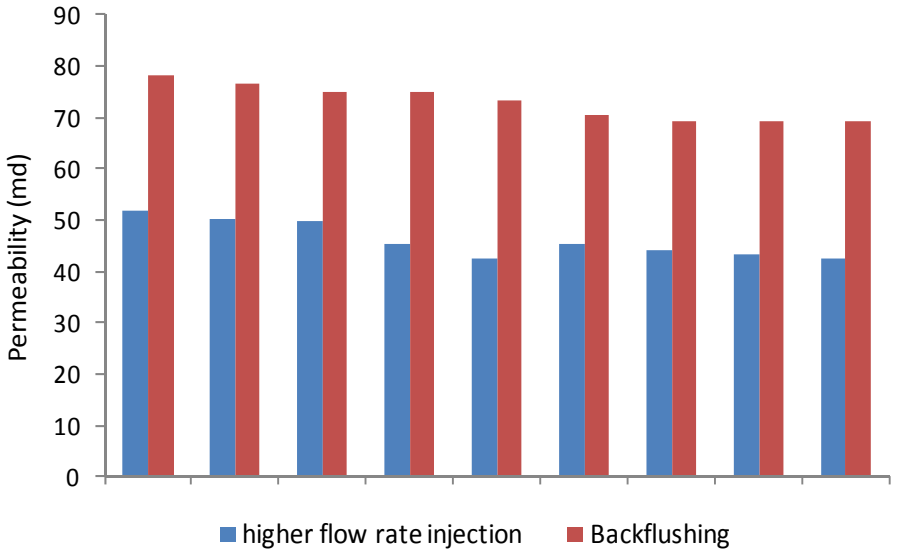

Figure 2.22: Comparison of permeability measurements during backflushing and injecting at higher flow rates. There was about 25 md difference.

Despite the permeability improvement during backflushing, silver nanoparticles were still not detected in the effluents. UV-vis analysis was conducted and optical density spectra were obtained. All effluent samples (from backflushing and injecting at higher flow rates) exhibited the behavior of pure water as shown in Figure 2.23. Effluents were examined by SEM imaging in which no images showed any sign of silver nanoparticles.

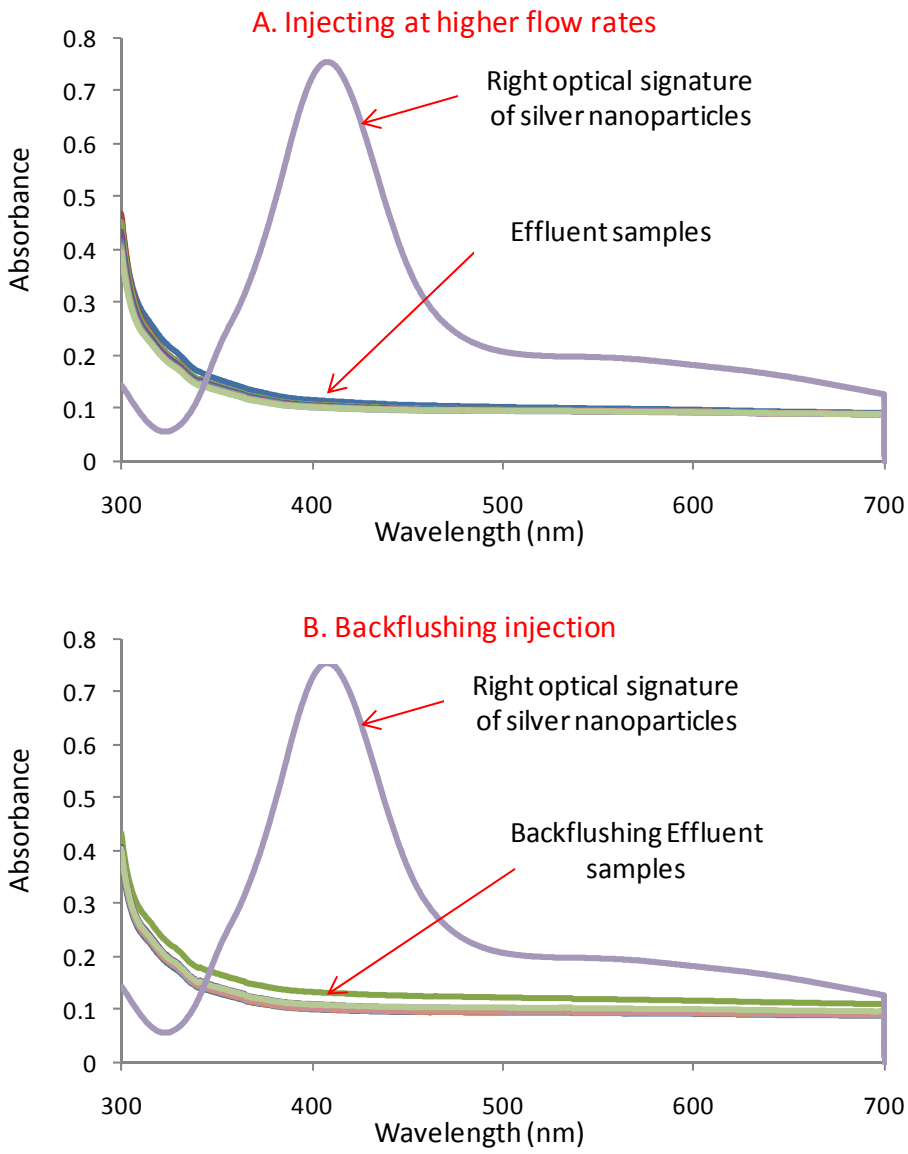

Figure 2.23: Optical density spectra of effluents collected during (A) post-injection at higher flow rate and (B) backflushing at the same rate.

2.8.3 Tin-bismuth injection results

Tin-bismuth nanoparticles were identified in a few effluent samples in low concentrations. It was observed that only nanoparticles with diameters 200 nm and smaller were transported within the pore spaces of the rock, as shown in the SEM image in Figure 2.24A. Note that the influent sample (Figure 2.10) contained nanoparticles as large as 600 nm. It was speculated that larger particles (greater than 200 nm) were trapped at the inlet of the core. In fact, SEM imaging of the backflushing effluents showed that there was entrapment and remobilization of various nanoparticle sizes, including the sizes greater

than 200 nm (Figure 2.24B). The rock filtered the injected nanofluid, allowing only certain particle sizes to flow through. It should be noted that this is a qualitative analysis in which the determination of the relative numbers of particles recovered was not possible.

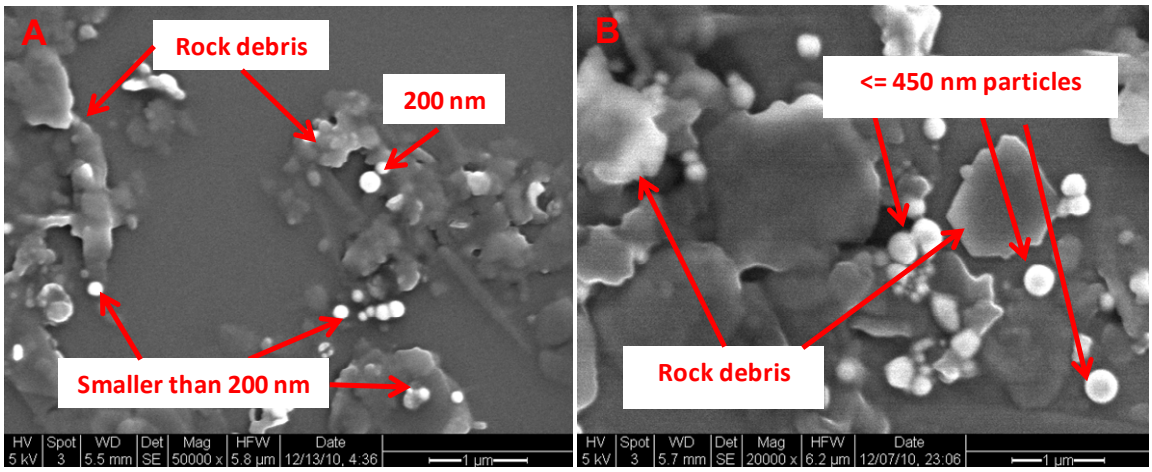

Figure 2.24: SEM imaging showing the tin-bismuth nanoparticles at the effluent during (A) injection and (B) backflushing of the Berea sandstone. Only particles smaller than 200 nm were transported through the pore spaces while larger particles were trapped at the inlet of the core and remobilized during backflushing.

The permeability measurements during the injection agree with this finding. The permeability as a function of the injected volume is depicted in Figure 2.25. There was a drop in permeability to about 56% of the original value, after which the permeability remained at that level during the first post-injected pore volume, indicating the partial plugging of the pores. Then, permeability started to increase until reaching a plateau at approximately 82% of its value prior to the nanofluid injection. At this time, only nanoparticles of 200 nm and smaller were observed in the effluent, using SEM (Figure 2.24A). As mentioned earlier, the backflushing of the core remobilized some particles and as a result the permeability of the rock improved slightly by 8% (i.e. back to 90% of its original value). However, permeability improvement (from 56% to 90% of original value) does not imply a good recovery of the injected nanoparticles. If the injected nanofluid has a visible color, it is possible to observe the nanoparticles in the effluent visually. In the case of the tin-bismuth injection, the influent had a dark gray color. All effluent samples appeared colorless and transparent, so it was hypothesized that many of the nanoparticles had been trapped within the rock pores, most likely at the inlet of the core. Examining the pore spaces of the rock itself confirmed that considerable numbers of the tin-bismuth nanoparticles were trapped (Figure 2.26).

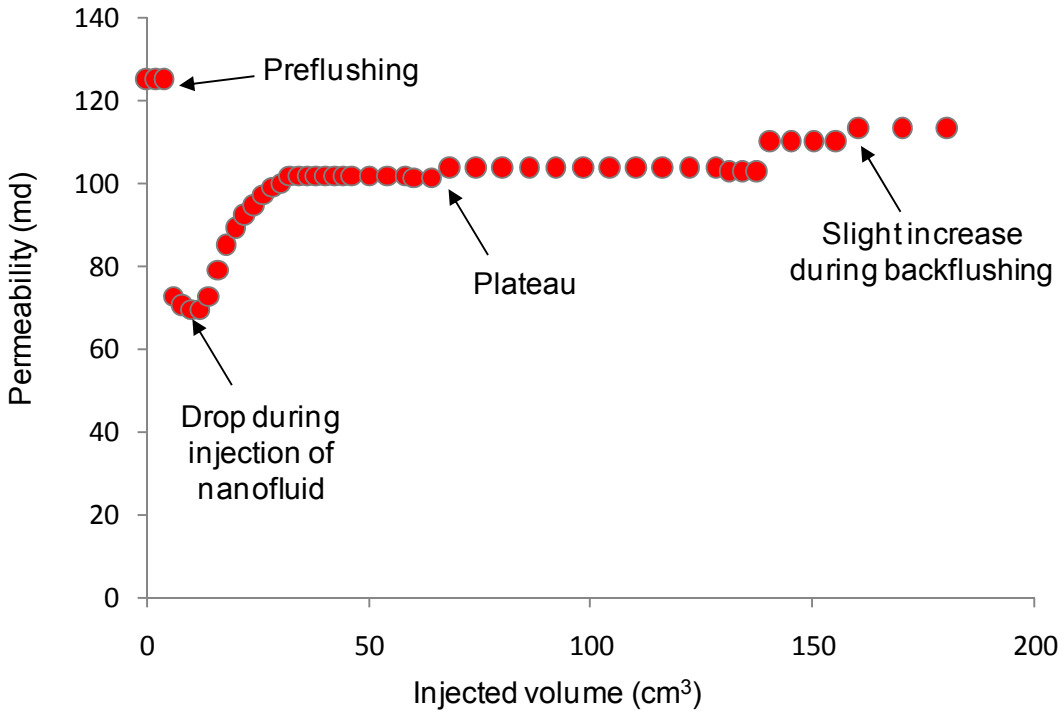

Figure 2.25: Permeability measurements during the injection of the tin-bismuth nanoparticles.

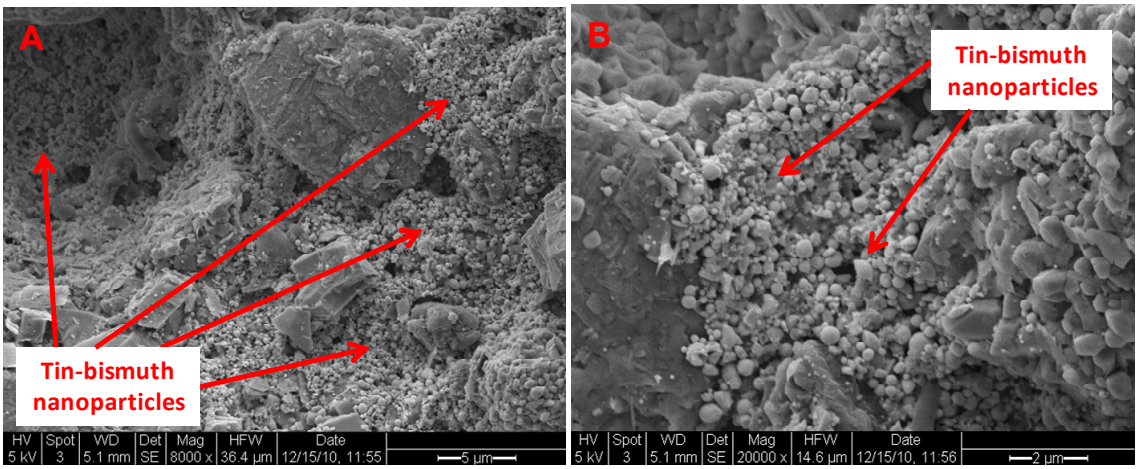

Figure 2.26: SEM image of (A) the pore space at the inlet of Berea sandstone used during the tin-bismuth injection, (B) at higher magnification. Nanoparticle entrapment is apparent.

Further evaluation of the rock pore spaces using SEM imaging (Figure 2.27) demonstrated the bridging and plugging of the tin-bismuth nanoparticles in the pore throat entry. Kanj et al. (2009) explained that high concentrations of small particles might bridge across the

pore throats. The authors also added that larger particles could result in direct plugging of the pore entry. Both phenomena would impact the rock permeability negatively. Particles shown in Figure 2.26 could not be mobilized either by increasing the injection flow rate or by backflushing and were probably responsible for the permanent reduction in the rock permeability.

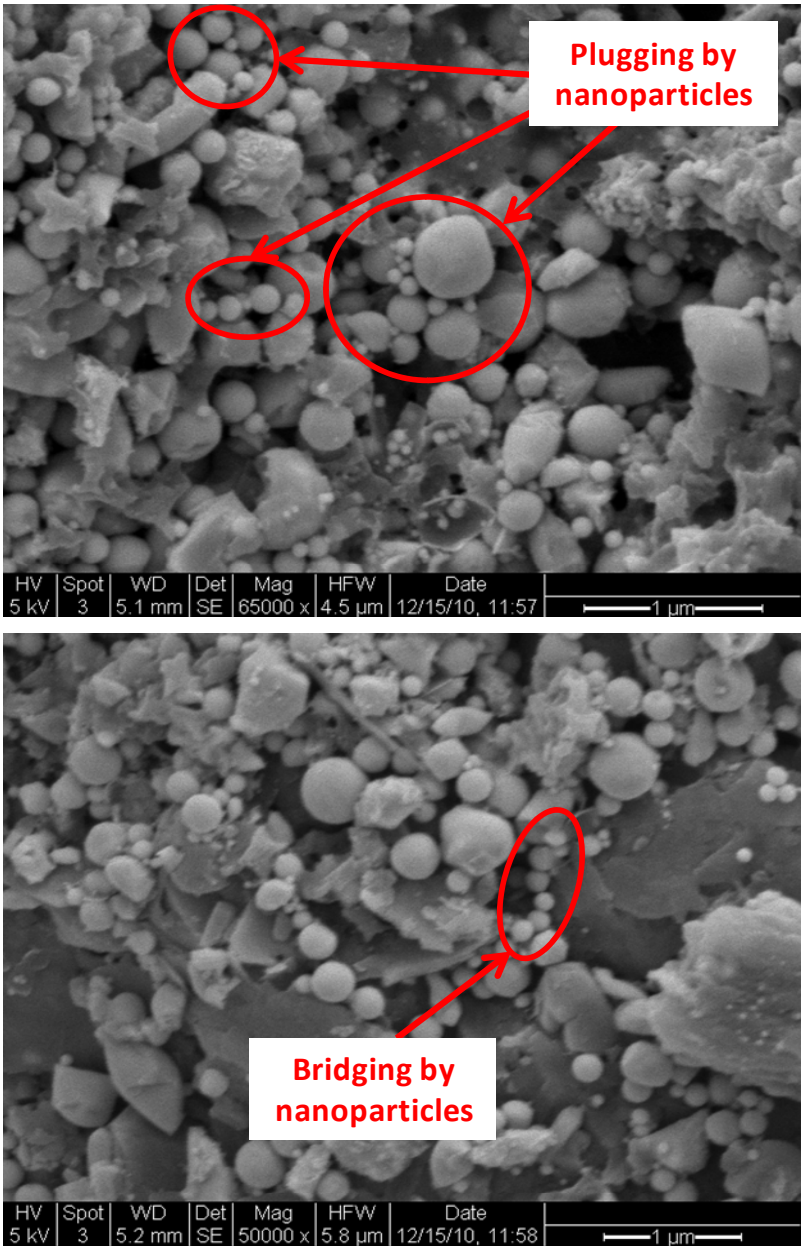

Figure 2.27: SEM images from within the pore spaces of the Berea sandstone, demonstrating the bridging and plugging phenomena.

The SEM analysis did not provide conclusive evidence of the mechanism of particle entrapment. Alaskar et al. (2010) reported that the nanoparticle shape and surface

characteristics play a major role in their transport through a porous medium. They also reported that the spherical silicon dioxide (SiO_2) nanoparticles with narrow size distribution and surface charge compatible with that of the rock were transported successfully through the pore spaces of Berea sandstone. SiO_2 nanoparticles were not trapped in the pore spaces by hydraulic, chemical or electrostatic effects. The tin-bismuth nanoparticles exhibit similar properties in terms of shape and surface charge (negatively charged), except that the tin-bismuth nanoparticles had a wider distribution of sizes between 50 to 600 nm (Figure 2.10). Thus, particle shape and surface charge should not have imposed flow constraints. The optimized testing program suggested by Kanj et al. (2009) emphasizes particle size, influent concentration and affinity of particles to rock matrix. In the case of tin-bismuth injection, although the influent sample had wide distribution of particle sizes, they were all within the size range of the pore network. Therefore, it was concluded that the tin-bismuth nanoparticles affinity and/or concentration may have caused their entrapment.

Further investigation of particle affinity to Berea sandstone was carried out by injecting the same influent sample with identical concentration into a slim tube packed with glass beads. This allowed testing the transport of the tin-bismuth nanoparticles in the absence of the rock core material. One pore volume of the nanofluid was injected at the rate of 0.5 cm^3/min followed by continuous injection of pure water at the same rate. Several effluent samples were collected and analyzed by SEM imaging. It was found that the tin-bismuth nanoparticles of all sizes flowed through the slim tube. The increasing concentration of the nanoparticles was observed visually through the injection of the first post-injected pore volume as illustrated in Figure 2.28. SEM imaging confirmed this finding as depicted in Figure 2.29.

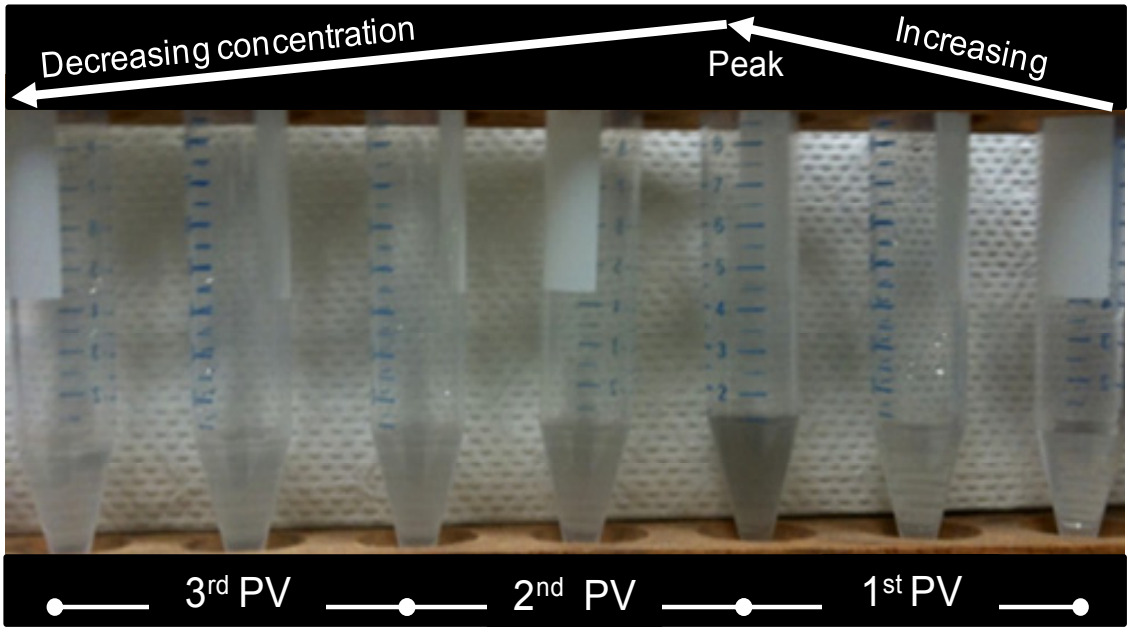

Figure 2.28: Visual characterization of effluent samples for their tin-bismuth nanoparticles content based on color.

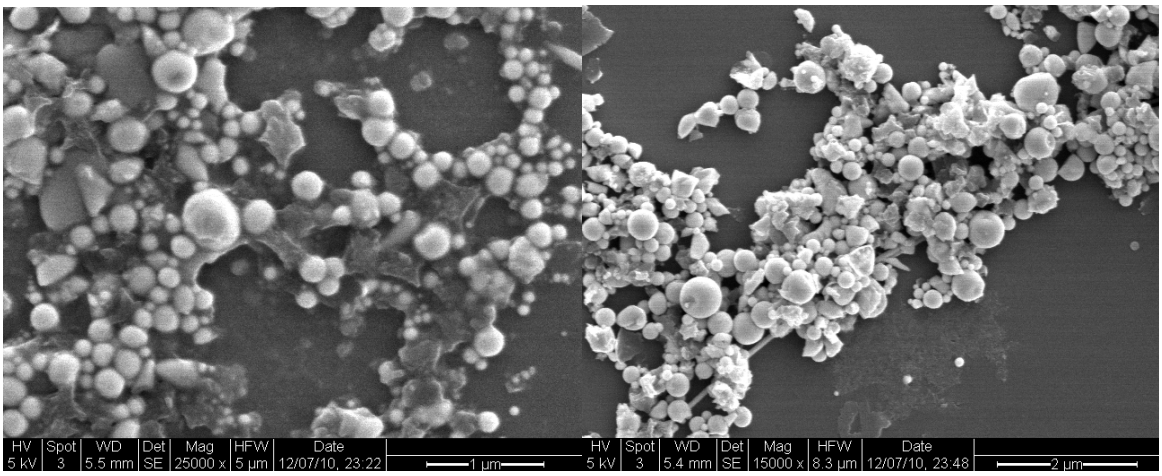

Figure 2.29: SEM images of the effluent collected during the injection of tin-bismuth nanoparticles into the slim tube packed with glass beads.

Thus, it has been demonstrated that the spherically shaped tin-bismuth nanoparticles can be recovered following their injection into tube packed with glass beads without being trapped within the flow conduits, but not through the pore network of the rock (which has much smaller pores). This might be attributed to an affinity of these nanoparticles to the sandstone rock matrix or high nanoparticle concentration imposing constraints to their flow. The complexity of the rock pore network compared the large pores between the glass beads was not taken into consideration during this analysis.

2.9 PROMISING NANOSENSOR CANDIDATES

In addition to the experimental work, a review of material science literature regarding temperature sensors revealed some other potential candidates for geothermal applications. Here we discuss two of the most promising candidates: dye-releasing silica nanoparticles with melting shells and time-temperature indicators.

2.9.1 Hollow silica nanoparticles with encapsulated dye and impermeable melting shells

As it is common practice to use fluorescent dyes as tracers in geothermal reservoirs, a dye-release temperature-sensing scheme would be a convenient means of measuring temperature. Additionally, if a thermally stable dye with sufficiently low detection limits were employed, this sensing scheme would eliminate the need for nanoparticle collection at the production well, which is a significant technical challenge.

Botterhuis et al. (2006) have synthesized hollow silica spheres with encapsulated dye and demonstrated controlled-release behavior in aqueous media. The dye release was found to exhibit two types of behavior: rapid release of dye immobilized in the meso- and macropores via diffusion, and slow, steady release of dye incorporated into the silica walls after the walls dissolved around it.

If these hollow silica nanoparticles were coated with a material impermeable to dye diffusion and with an appropriate melting point, temperature-sensitive dye release could be achieved for geothermal applications, as illustrated in Figure 2.30. Possible candidates for the coating material include tin-bismuth and polymers with melting points in the temperature range of geothermal interest.

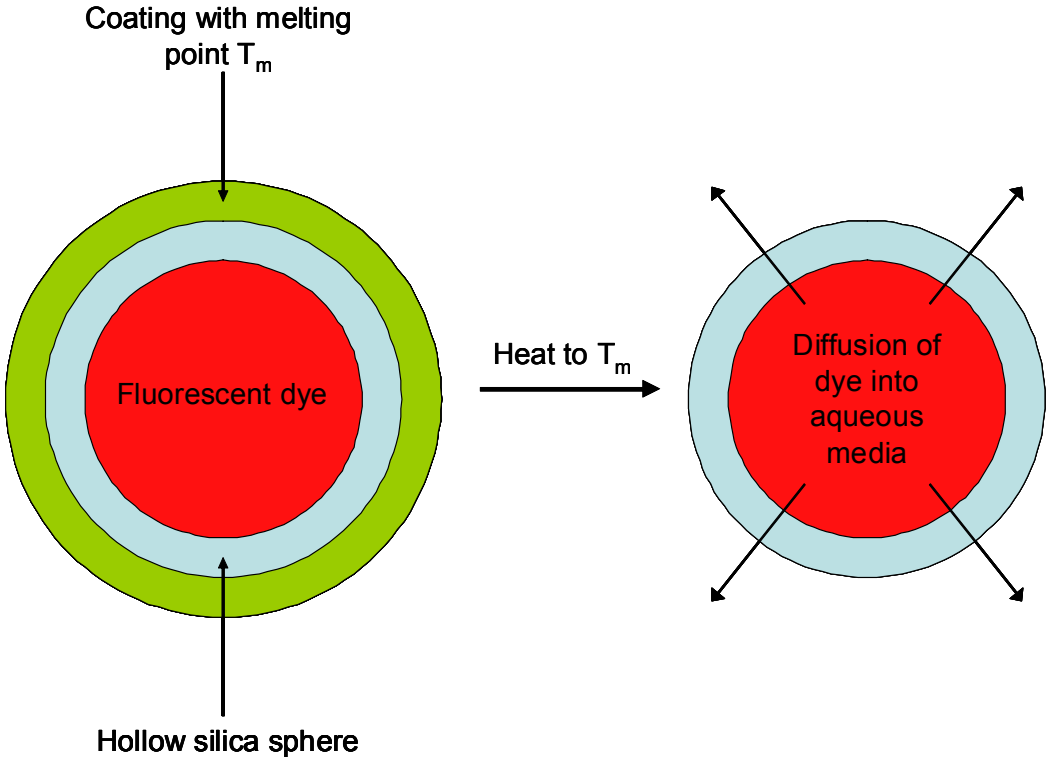

Figure 2.30: Cartoon of dye-release scheme triggered by the melting of an impermeable shell.

Technical challenges anticipated include development of a suitable coating process, the precision of temperature measurement, and particle mobility in reservoir rock. Before addressing these challenges, we intend to develop a proof of concept using a coating that is sensitive in a lower temperature regime.

2.9.2 Time-temperature indicators

Sing, Weder, and Kunzelman (2009) have developed time-temperature indicators (TTIs) that have been demonstrated to work in high temperature regimes (130°C – 200°C). As most temperature sensors described in the literature operate at lower temperature ranges found in biomedical applications, these sensors are perhaps the most promising of those reviewed. These TTIs are films of dye/polymer blends that undergo irreversible fluorescence changes when heated above the glass transition temperature T_g of the polymer, as illustrated in Figure 2.31.

In the reviewed work, the dyes 4,4'-bis(2-benzoxazolyl)stilbene or cyano-substituted oligo(*p*-phenylene vinylene) were kinetically trapped in thermodynamically unstable dispersed states within ethylene/norbornene copolymers by quenching the blend below T_g during synthesis. Heating the TTIs above T_g caused irreversible phase separation to occur by means of dye aggregation. This aggregation allowed excimers to form and charge-transfer interactions to occur, resulting in permanent changes in fluorescence.

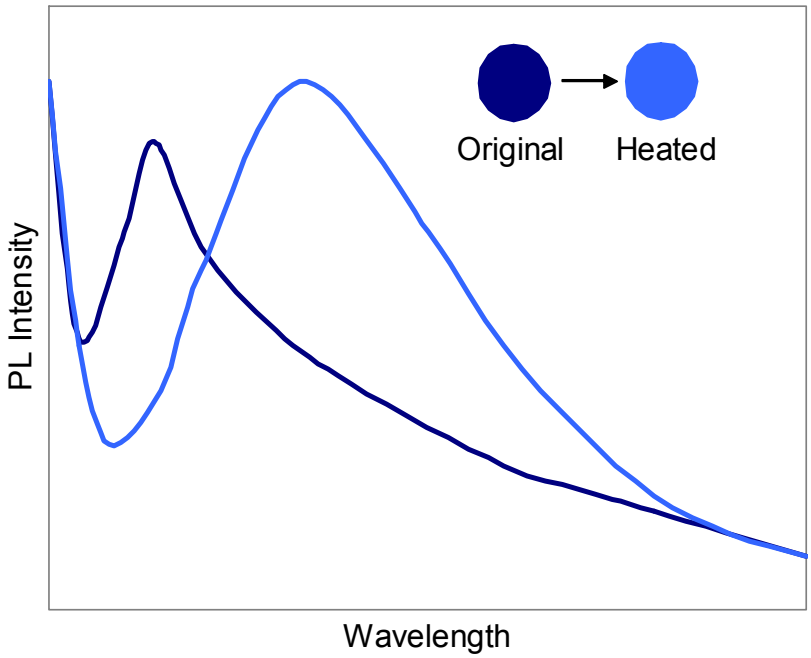

Figure 2.31: Cartoon of permanent photoluminescence (PL) emission spectral shift that occurs upon heating of TTIs, as shown by Sing, Weder, and Kunzelman (2009).

The kinetics of dye aggregation upon heating exhibited predictable behavior, with the kinetic rate constant following Arrhenius-type temperature dependence. Moreover, the time scale of aggregation can be tuned between seconds and days by changing the dye concentration, choice of dye, or choice of host polymer. Thus, TTIs show potential for providing information about the time of exposure to a given temperature, which could be used to estimate the location of the thermal front within a geothermal reservoir.

We anticipate three main technical challenges regarding the development of TTIs for geothermal applications. The first is the synthesis of nano- or microparticles of the dye-polymer blends with the same capabilities, as the sensors described by Sing, Weder, and Kunzelman (2009) are films, not particles. The second is the precision with which such a sensor can measure reservoir temperature. The third is particle mobility through reservoir rock. We aim to address these challenges and evaluate this candidate according to a full set of criteria in future work.

2.10 FUTURE WORK

The next stage will be to separate the tin-bismuth nanoparticles into a monodisperse and more uniform sample with narrower size distribution. The monodisperse sample will be injected into Berea sandstone for further investigate of the effect of wide size distribution on the transport of tin-bismuth nanoparticles.

Flow of microspheres in fractured rocks is also planned. A fractured greywacke rock sample will be used. Microspheres of different sizes will be injected through the fracture and effluent samples will be collected. Fracture properties such as size and shape may be inferred from the production history of those microspheres. Ultimately, it is planned to obtain samples of dye-releasing particles and time-temperature indicators in order to broaden the investigation of temperature sensors to a group of candidates.

3. FRACTURE CHARACTERIZATION USING RESISTIVITY

This research project is being conducted by Research Assistant Lilja Magnusdottir, Senior Research Engineer Kewen Li and Professor Roland Horne. The objective of this project is to investigate ways to use resistivity to infer fracture properties in geothermal reservoirs.

3.1 SUMMARY

The aim of this project is to use resistivity measurements and modeling to characterize fracture properties in geothermal fields. The resistivity distribution in the field can be estimated by measuring potential differences between various points and the resistivity data can be used to infer fracture properties due to the large contrast in resistivity between water and rock.

A two-dimensional model has been developed to calculate a potential field due to point sources of excitation. The model takes into account heterogeneity by solving the potential field for inhomogeneous resistivity. Fractures are modeled as areas with resistivity different from the rock, to investigate the changes in the potential field around them. The grid is rectangular and nonuniform so the fracture elements can be modeled smaller than the elements for the rest of the reservoir, in order to decrease the total number of elements. Flow simulations have been performed of a conductive fluid injected into a reservoir to enhance the difference in resistivity between fractures and rock, and the potential difference has been calculated between two wells as a function of time as the fluid flows through the fractured rock. Previous results for a simple fracture network showed that the time history of voltage differences correspond to the fracture networks and therefore have shown promising possibilities in indicating fracture locations and character. This time, fractured rock was modeled in one corner of a reservoir and then in the opposite corner, to study the difference in time history of voltage differences between these two cases.

Future work includes studying further the relationship between fracture networks and the change in potential differences as conductive tracer is injected into the reservoir. Another future goal is to study the possibility of using the potential differences with inverse modeling to characterize fracture patterns.

3.2 INTRODUCTION

In an Enhanced Geothermal System (EGS) application, the configuration of the fractures is central to the performance of the system. Therefore fracture characterization is important to design the recovery strategy appropriately and thereby to optimize the overall efficiency of geothermal energy recovery.

The goal of this study is to find ways to use Electrical Resistivity Tomography (ERT) to characterize fractures in geothermal reservoirs. ERT is a technique for imaging the resistivity of a subsurface from electrical measurements. Pritchett (2004) concluded based on a theoretical study that hidden geothermal resources can be explored by electrical resistivity surveys because geothermal reservoirs are usually characterized by substantially reduced electrical resistivity relative to their surroundings. Electrical current moving through the reservoir passes mainly through fluid-filled fractures and pore spaces because the rock itself is normally a good insulator. In these surveys, a direct current is sent into the

ground through electrodes and the voltage differences between them are recorded. The input current and measured voltage difference give information about the subsurface resistivity, which can then be used to infer fracture locations.

Resistivity measurements have been used in the medical industry to image the internal conductivity of the human body, for example to monitor epilepsy, strokes and lung functions as discussed by Holder (2004). In Iceland, ERT methods have been used to map geothermal reservoirs. Arnarson (2001) describes how different resistivity measurements have been used effectively to locate high temperature fields by using electrodes located on the ground's surface. Stacey et al. (2006) investigated the feasibility of using resistivity to measure saturation in a rock core. A direct current pulse was applied through electrodes attached in rings around a sandstone core and it resulted in data that could be used to infer the resistivity distribution and thereby the saturation distribution in the core. It was also concluded by Wang and Horne (2000) that resistivity data have high resolution power in the depth direction and are capable of sensing the areal heterogeneity.

In the approach considered in this project so far, electrodes would be placed inside two geothermal wells (future work will involve studying different electrode arrangements with a greater number of wells) and the potential differences between them studied to locate fractures and infer their properties. Due to the limited number of measurement points, the study is investigating ways to enhance the process of characterizing fractures from sparse resistivity data. For example, in order to enhance the contrast in resistivity between the rock and fracture zones, a conductive tracer would be injected into the reservoir and the time-dependent voltage difference measured as the tracer distributes through the fracture network.

Slater et al. (2000) have shown a possible way of using Electrical Resistivity Tomography (ERT) with a tracer injection by observing tracer migration through a sand/clay sequence in an experimental $10 \times 10 \times 3$ m^3 tank with cross-borehole electrical imaging. Singha and Gorelick (2005) also used cross-well electrical imaging to monitor migration of a saline tracer in a $10 \times 14 \times 35$ m^3 tank. In previous work, usually many electrodes were used to obtain the resistivity distribution for the whole field at each time step. The resistivity distribution was then compared to the background distribution (without any tracer) to see resistivity changes in each block visually, to locate the saline tracer and thereby the fractures. Using this method for a whole reservoir would require a gigantic parameter space, and the inverse problem would not likely be solvable, except at very low resolution. However, in the method considered in this study, the potential difference between the wells would be measured and plotted as a function of time while the conductive tracer flows through the fracture network. Future work will involve using that response, i.e. potential difference vs. time, in an inverse modeling process to characterize the fracture pattern.

First the theory behind the resistivity model is defined. Then, simulations are described in which the potential differences were calculated for two cases while a conductive fluid was injected into the reservoir. Finally, future work is outlined.

3.3 RESISTIVITY MODELING

One of the main problems in resistivity modeling is to solve the Poisson equation that describes the potential field and to complete the inversion iteration efficiently. That governing equation can be derived from basic electrical relationships as described by Dey and Morrison (1979). Ohm's Law defines the relationship between current density, J, conductivity of the medium, σ, and the electric field, E, as:

$$J = \sigma E \tag{3.1}$$

The stationary electric fields are conservative, so the electric field at a point is equal to the negative gradient of the electric potential there, i.e.:

$$E = -\nabla \phi \tag{3.2}$$

where ϕ is the scalar field representing the electric potential at the given point. Hence,

$$J = -\sigma \nabla \phi \tag{3.3}$$

Current density is the movement of charge density, so according to the continuity equation, the divergence of the current density is equal to the rate of change of charge density,

$$\nabla J = \frac{\partial Q(x,y,z)}{\partial t} = q(x,y,z) \tag{3.4}$$

where q is the current density in amp m^{-3}. Combining equations (3.3) and (3.4) gives the following Poisson's equation which describes the potential distribution due to a point source of excitation,

$$\nabla[\sigma \nabla \phi] = -q(x,y,z) \tag{3.5}$$

The conductivity σ is in mhos m^{-1} and the electric potential is in volts. This partial differential equation can then be solved numerically for the resistivity problem.

3.3.1 Finite Difference Equations in Two Dimensions

Finite difference method is used to approximate the solution to the partial differential equation (3.5) using a point-discretization of the subsurface (Mufti, 1976). The computational domain is discretized into $Nx \times Ny$ blocks and the distance between two adjacent points on each block is h in x-direction and l in y-direction, as shown in Figure 3.1.

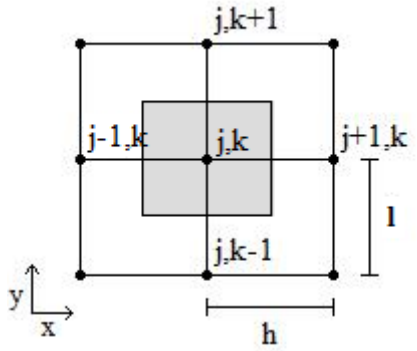

Figure 3.1: Computational domain, discretized into blocks.

Taylor series expansion is used to approximate the derivatives of equation (3.5) about a point (*j,k*) on the grid,

$$\left.\frac{\partial}{\partial x}\left(\sigma\frac{\partial\phi}{\partial x}\right)\right|_{(j,k)} \approx \frac{\left[\begin{array}{l}\phi(j+1,k)\sigma\left(j+\frac{1}{2},k\right)+\phi(j-1,k)\sigma\left(j-\frac{1}{2},k\right)\\ -\left[\sigma\left(j+\frac{1}{2},k\right)\sigma\left(j-\frac{1}{2},k\right)\right]\phi(j,k)\end{array}\right]}{h^2} \tag{3.6}$$

$$\left.\frac{\partial}{\partial y}\left(\sigma\frac{\partial\phi}{\partial y}\right)\right|_{(j,k)} \approx \frac{\left[\begin{array}{l}\phi(j,k+1)\sigma\left(j,k+\frac{1}{2}\right)+\phi(j,k-1)\sigma\left(j,k-\frac{1}{2}\right)\\ -\left[\sigma\left(j,k+\frac{1}{2}\right)\sigma\left(j,k-\frac{1}{2}\right)\right]\phi(j,k)\end{array}\right]}{l^2} \tag{3.7}$$

The point (*j,k*) represents the shaded area in Figure 3.1 (area = *hl*) so the current density due to an electrode at that point is given by,

$$q(j,k)=\frac{I}{hl} \tag{3.8}$$

where *I* [amp] is the current injected at point (*j,k*) Combining Equations (3.5)-(3.8) and solving for the electric potential ϕ at point (*j,k*) gives,

$$\phi(j,k)=\frac{\left[Ihl+\phi(j+1,k)c_1l^2+\phi(j-1,k)c_2l^2+\phi(j,k+1)c_3h^2+\phi(j,k-1)c_4h^2\right]}{\left[c_1+c_2\right]l^2+\left[c_3+c_4\right]h^2} \tag{3.9}$$

The parameters c_i represent the conductivity averaged between two adjacent blocks, i.e.

$$c_1=\frac{2}{\rho(j,k)+\rho(j+1,k)} \tag{3.10}$$

$$c_2=\frac{2}{\rho(j,k)+\rho(j-1,k)} \tag{3.11}$$

$$c_3=\frac{2}{\rho(j,k)+\rho(j,k+1)} \tag{3.12}$$

$$c_4=\frac{2}{\rho(j,k)+\rho(j,k-1)} \tag{3.13}$$

where ρ(*j,k*) is the resistivity [ohm-m] of the node at grid coordinates *j,k*.

3.3.2 Iteration method

In order to solve Equation (3.9) numerically and obtain the results for electrical potential ϕ at each point on the grid, the iteration method called Successive Over-Relaxation was used (Spencer and Ware, 2009). At first, a guess is made for $\phi(j,k)$ across the whole grid, for example $\phi(j,k)$= for all *j,k*. That guess is then used to calculate the right hand side of Equation (3.9) (Rhs) for each point and the new set of values for $\phi(j,k)$ is calculated using the following iteration scheme,

$$\phi_{n+1}=\omega Rhs+(1-\omega)\phi_n \tag{3.14}$$

The multiplier ω is used to shift the eigenvalues so the iteration converges better than simple relaxation. The number ω is between 1 and 2, and when the computing region is rectangular the following equation can be used to get a reasonable good value for ω,

$$\omega = \frac{2}{1+\sqrt{1-R^2}} \tag{3.15}$$

where:

$$R = \frac{\left(\cos\left(\frac{\pi}{Nx}\right)+\cos\left(\frac{\pi}{Ny}\right)\right)}{2} \tag{3.16}$$

The natural Neumann boundary condition is used on the outer boundaries, i.e. $\frac{\partial \phi}{\partial n} = 0$.

3.4 RESULTS

A flow simulation was performed using TOUGH2 reservoir simulator to see how a tracer, which increases the conductivity of the fluid, distributes after being injected into the reservoir. The simulation was carried out on a two-dimensional grid with dimensions 1000 × 1000 × 10 m^3 with fractured rock modeled as a squared area (green blocks), first in the lower right corner as shown in Figure 3.2, and then in the upper left corner as shown in Figure 3.3.

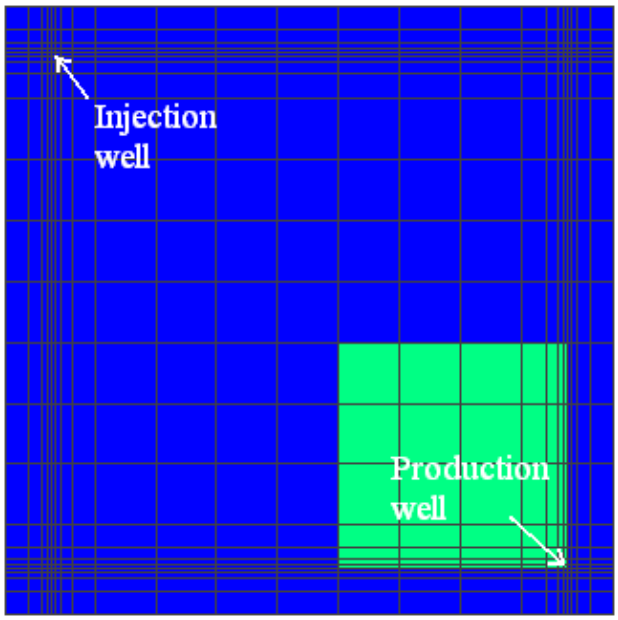

Figure 3.2: Fractured rock (green blocks) modeled in the lower right corner of the reservoir.

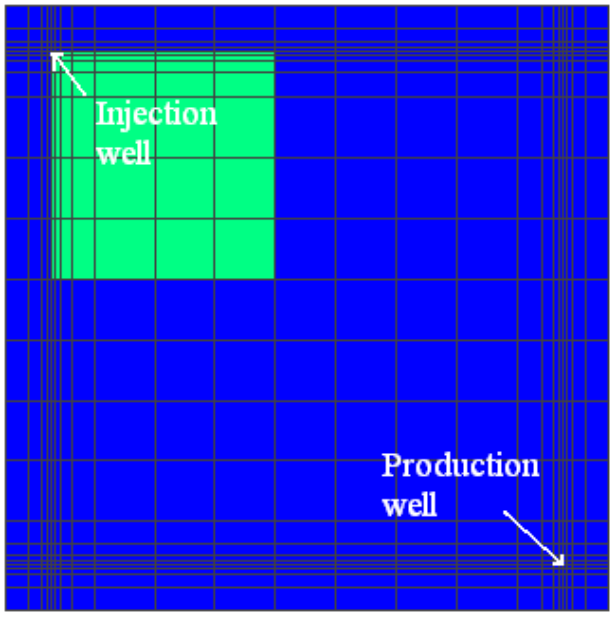

Figure 3.3: Fractured rock (green blocks) modeled in the upper left corner of the reservoir.

The goal was to study the difference in potential field between these two cases as conductive fluid is injected into the reservoir. The reservoir is modeled with porosity 0.4 and permeability 10^5 md (10^{-10} m^2) while the fractured rock has porosity 0.65 and permeability $5\cdot\times 10^{10}$ md ($5\cdot\times 10^{-5}$ m^2).

No-flow boundary conditions were used as before, and 100 kg/s of water was injected in the upper left corner with enthalpy 100 kJ/kg, and 0.1 kg/s of tracer with enthalpy 100 kJ/kg. The production well was set to produce at a constant pressure, 8 bar. The initial pressure was set to 9.6 bar, temperature to 150°C and initial tracer mass fraction to 10^{-9} because the simulator could not solve the problem with zero initial tracer mass fraction.

The following equation was used to calculate the electrical conductivity, $1/\rho_w$, of a NaCl water solution (Crain, 2010),

$$\rho_w = \frac{400{,}000}{\left(\frac{9}{5}T + 32\right)Ws} \tag{3.17}$$

in order to define conductivity values in the resistivity model as NaCl tracer flows through the reservoir. T is the formation temperature (assumed to be 150°C) and Ws is the water salinity [ppm NaCl].

The resistivity for the rock before fluid had been injected was set as 100 Ωm for the fractured area (assuming fractures were filled with water) and as 2000 Ωm for the rest of the reservoir. Figures 3.4 and 3.5 show how the potential difference between the injector and the producer changes with time for the reservoirs shown in Figure 3.2 and 3.3.

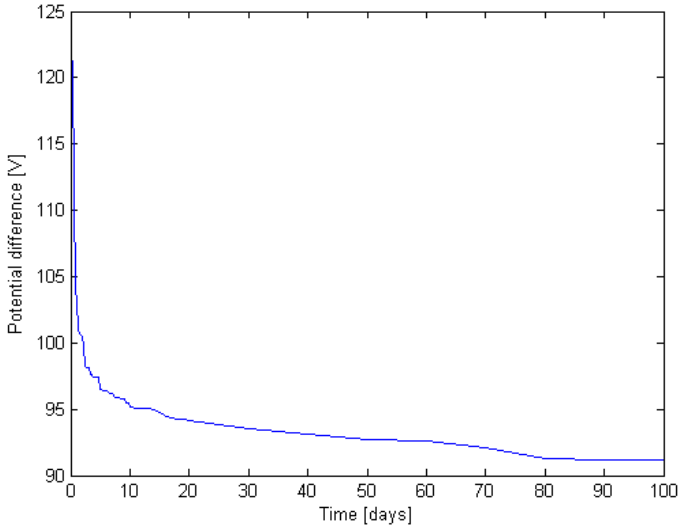

Figure 3.4: Potential difference between injection and production wells for reservoir in Figure 3.2.

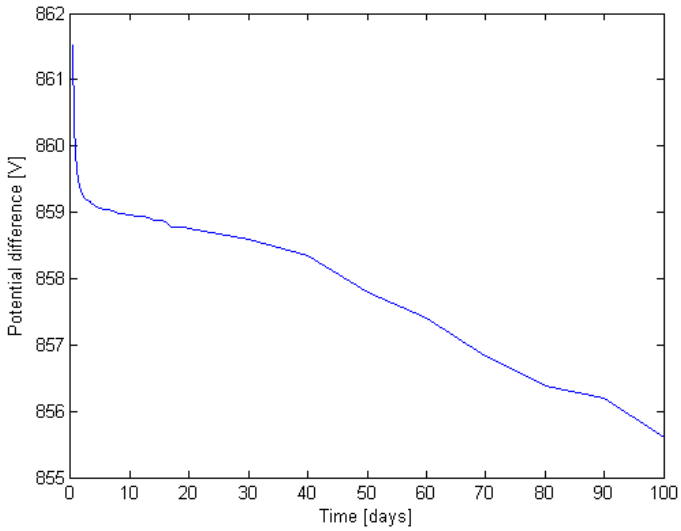

Figure 3.5: Potential difference between injection and production wells for reservoir in Figure 3.3.

The potential difference in the graph in Figure 3.4 drops very rapidly for the first 10 days, but then decreases more slowly when the tracer front has reached the fractured area. In Figure 3.5, the potential difference drops more slowly, as the conductive fluid first fills up the fractured rock, modeled with much higher porosity then the rest of the reservoir. More cases need to be studied, and probably run for a longer time period, in order to understand the correspondence between the changes in potential differences and fracture networks. But these preliminary results indicate that different fracture properties give different potential difference histories between two wells, and could therefore be used to indicate fracture characteristics.

3.5 FUTURE WORK

The results have shown that the resistivity model has promising possibilities in fracture characterization when used with a flow simulation of a conductive tracer. One of the next steps is to calculate the potential difference for more realistic fracture patterns, to study the correspondence between the potential difference and the fracture network. Other future goals are to use the resistivity model and flow simulations with inverse modeling to estimate the dimensions and topology of a fracture network. The objective is to develop a method which can be used to find where fractures are located and the character of their distribution.

In inverse modeling the results of actual observations are used to infer the values of the parameters characterizing the system under investigation. In this study, the output parameters would be the potential differences between wells as a function of time and the input parameters would include the dimensions and orientations of the fractures between the wells. The objective function measures the difference between the model calculation (the calculated voltage difference between the wells) and the observed data (measured potential field between actual wells), as illustrated in Figure 3.6, and a minimization algorithm proposes new parameter sets that improve the match iteratively.

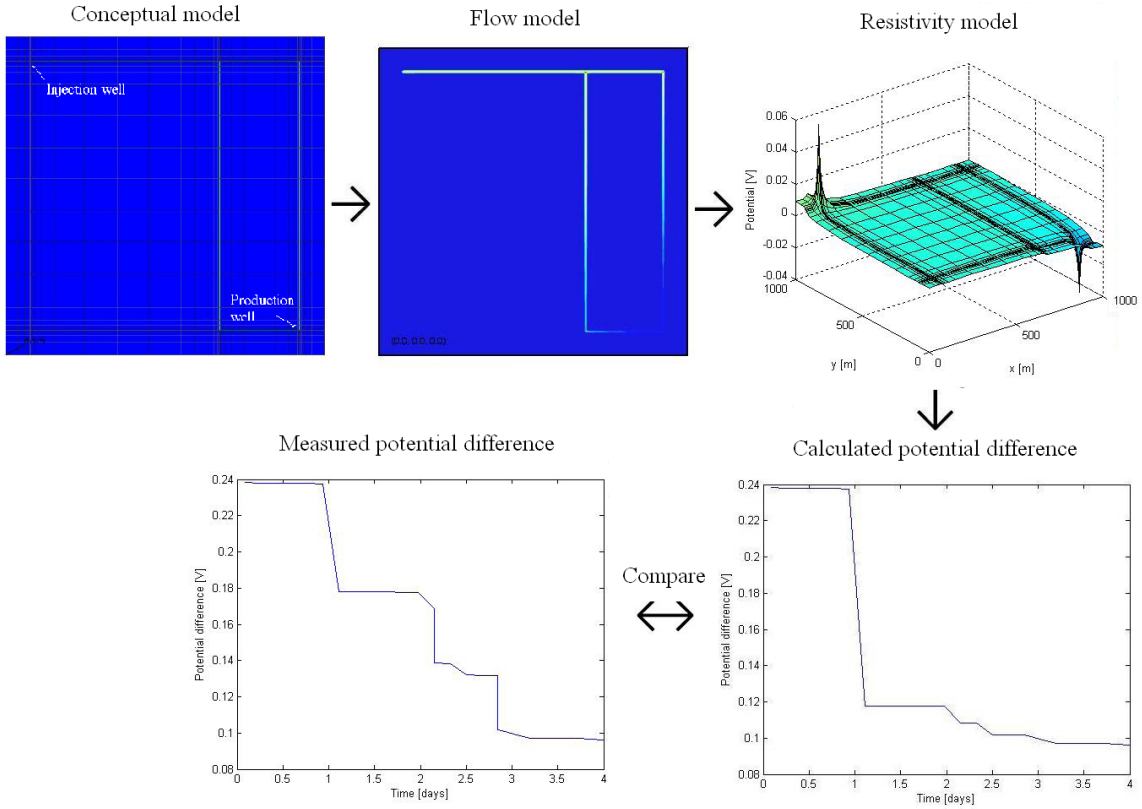

Figure 3.6: The inverse problem; the calculated potential difference is compared to the measured potential difference and the inverse problem solved to characterize fracture patterns.

The possibility of using fewer wells and different well arrangements will be studied to estimate the minimum number of measurement locations necessary to solve the problem.

4. FRACTURE APERTURE DETERMINATION USING THERMAL AND TRACER DATA

This research project is being conducted by Research Associate Carla Kathryn Co and Professor Roland Horne. The objective of this study is to develop a methodology to estimate fracture dimensions based on thermal breakthrough and tracer return data.

4.1 SUMMARY

This study aims to determine an effective fracture aperture using tracer concentration and thermal breakthrough profiles. A single fracture was used to represent the connectivity between injection and production well pairs. An analytical model derived by Gringarten and Sauty (1975) was used to estimate the fracture aperture from thermal breakthrough time and mean tracer arrival time. Estimated fracture aperture values ranged from 2.2 to 14.3 mm, which is consistent with the value (2 mm) derived from finite element heat and mass (FEHM) modeling. As the preliminary study shows promising results, further analysis and numerical simulation will be undertaken.

4.2 INTRODUCTION

Fracture aperture is an important parameter in geothermal reservoirs. Fracture aperture influences transport and thermal behavior of the reservoir, both in EGS and in conventional hydrothermal systems. An important application is the determination of the degree of interwell connectivity. Of critical importance is the prevention of thermal breakthrough from injection wells to production wells. During the 1980s, several unsuccessful attempts we made to estimate fracture aperture by matching tracer test data. This was because the parameter estimation problem has multiple degrees of freedom, which makes it difficult to separate fracture aperture from other unknown reservoir parameters. To constrain the degrees of freedom, thermal response data could be used. This was proposed in the 1980s, however at the time no data existed that provided both tracer and thermal responses. Now that several EGS and fractured reservoirs have been monitored to provide these data, the possibility now exists to estimate fracture aperture in those fields. In this project, a single fracture model was used to describe the connectivity of an injection and production well pair. Tracer and thermal data were used to estimate the fracture width for this simplified model.

The main objective of the work done this quarter is to determine whether it would be feasible to derive reasonable estimates for the fracture aperture using both thermal and tracer test results. A secondary objective is to document existing analytical models and field data available in literature. Furthermore, the fracture width values calculated are compared to those derived from other datasets to check for consistency.

4.3 METHODOLOGY

4.3.1 Analytical Model

Gringarten and Sauty (1975) derived a solution that can be used for unsteady-state one-dimensional heat transfer through a fracture. The solution was similar to that for a porous medium, derived by Lauwerier (1955). The solution assumes a thin, uniform reservoir with an adiabatic boundary. Heat is transferred by conduction from the rock layers and the entering fluid. Since no mixing is assumed, the result is a stream-like channel flow.

Horne (1996) derived the resulting analytical solution for this model as Equation 4.1 where t_c is the tracer front arrival time, t_{th} is the thermal breakthrough time, and b is the fracture aperture. On the left hand side of Equation 4.1 is the relative temperature ratio. Here, T_o is the original reservoir temperature, T_w is the reservoir temperature at x, and T_{inj} is the injected fluid temperature. Thus, the fracture aperture can be determined using the thermal and tracer breakthrough data. Knowledge of the fracture aperture can then be used to predict temperature drawdown in producing wells.

$$\frac{T_o - T_w}{T_o - T_{inj}} = erfc\left\{\left[\frac{(\rho_w C_w)^2}{K_r \rho_r C_r}\left(\frac{b}{t_c}\right)^2 (t_{th} - t_c)\right]^{-\frac{1}{2}}\right\} \tag{4.1}$$

$$0.476 = \left[\frac{(\rho_w C_w)^2}{K_r \rho_r C_r}\left(\frac{b}{t_c}\right)^2 (t_{th} - t_c)\right]^{-\frac{1}{2}} \tag{4.2}$$

$$0.289 = \left[\frac{(\rho_w C_w)^2}{K_r \rho_r C_r}\left(\frac{b}{t_c}\right)^2 (t_{th} - t_c)\right]^{-\frac{1}{2}} \tag{4.3}$$

These are the analytical expressions used to model a single fracture connection between an injector and producer well pair. Equation 4.2 calculates the thermal arrival time t_{th} based on the assumption that the thermal front is characterized by a relative temperature ratio of 0.5 while Equation 4.3 assumes a ratio of 0.75. A similar equation was derived by Pruess and Bodvarsson (1984) where a relative temperature ratio of 0.75 was also used.

4.3.2 Available field data

Results from tracer tests in EGS and conventional fractured geothermal reservoirs have been reported frequently in the literature. However, thermal breakthrough data are not as widely published. For EGS fields, thermal data were obtained usually from long-term circulation tests, as for example in Hijiori, Matsunaga et al. (2002) and Matsunaga et al. (2005). Historic silica geothermometer data were used from Palinpinon field which is a conventional liquid-dominated reservoir, Maturgo at al. (2010). Matsukawa is a conventional vapor-dominated field, Fukuda at al. (2006). Table 4.1 provides a summary of the field data used in this study.

Table 4.1: Thermal and tracer breakthrough times from field data.

Field	***Injector***	***Producer***	t_c	t_{th}	***Source***
			days	*days*	
Hijiori	*HDR-1*	*HDR-2A*	*1*	*180*	*Matsunaga et al.*
	HDR-1	*HDR-3*	*4*	*250*	*(2002)*
					Matsunaga at al. (2005)
Palinpinon	*NJ2RD*	*NJ5D*	*15*	*365*	*Maturgo at al. (2010)*
	SG2RD	*NJ3D*	*28*	*365*	
Matsukawa	*M-6*	*M-8*	*1.5*	*146*	*Fukuda at al. (2006)*

4.4 PRELIMINARY CALCULATIONS AND RESULTS

As described in the previous section, fracture aperture can be estimated directly from the thermal and tracer breakthrough time. Assumptions for the values of the other parameters are listed in Table 4.2. These were the values assigned to these properties in the estimation of fracture aperture. Estimated fracture aperture values for the two relative temperature ratios are given in Table 4.3.

Table 4.2: Assumptions used in calculations

Rock thermal conductivity	K_r	*2*	*W/m-C*
Rock density	ρ_r	*2200*	*kg/m^3*
Water density	ρ_w	*900*	*kg/m^3*
Rock heat capacity	C_r	*0.712*	*kJ/kg-C*
Water heat capacity	C_w	*4.342*	*kJ/kg-C*

Table 4.3: Calculated fracture aperture from thermal and tracer breakthrough times.

			$\frac{T_o - T_w}{T_o - T_{inj}} = 0.5$	$\frac{T_o - T_w}{T_o - T_{inj}} = 0.75$
Field	***Injector***	***Producer***	***Calculated* b**	***Calculated* b**
			mm	*mm*
Hijiori	*HDR-1*	*HDR-2A*	*2.2*	*3.7*
	HDR-1	*HDR-3*	*3.8*	*6.3*
Palinpinon	*NJ2RD*	*NJ5D*	*6.1*	*10.3*
	SG2RD	*NJ3D*	*8.5*	*14.3*
Matsukawa	*M-6*	*M-8*	*3.0*	*5.0*

The estimates of fracture aperture *b* vary from 2.2 mm to 14.3 mm. Finite element heat and mass transfer modeling (FEHM) of the Hijiori field yielded an average fracture aperture value of 2 mm (Tenma et al., 2005). This is slightly less than the lowest estimated aperture value here, but considering the number of assumptions used in this method it is a

good agreement. It can be observed that the range of values obtained for both relative ratios is small. This means that a relative temperature ratio range of 0.5 to 0.75 will yield similar fracture aperture values.

4.6 FUTURE WORK

These preliminary calculations show promising results. Further analysis on this approach to estimating fracture aperture will be undertaken. Numerical simulation will be used to model the effect of fracture aperture on mass and heat transport. A discrete fracture network model will be used to model single fracture and fracture network connections between wells.

5. REFERENCES

Alaskar, M., Ames, M., Horne, R.N., Li, K., Connor, S. and Cui, Y.: "In-situ Multifunction Nanosensors for Fractured Reservoir Characterization," GRC Annual Meeting, Sacramento, USA, vol. 34 (2010).

Arnason, K.: Viðnámsmælingar í Jarðhitarannsóknum á Íslandi, Orkustofnun, Orkuþing (2001).

Bear, J., *Dynamics of fluids in porous media*, (1972), Dover.

Botterhuis, N., Sun, Q., Magusin, P., Santen, R. and Sommerdijk, N.: "Hollow Silica Spheres with an Ordered Pore Structure and Their Application in Controlled Release Studies," *Chem. Eur. J.* 2006, **12**, 1448-56.

Chen, H., Li, Z., Wu, Z. and Zhang, Z.: "A novel route to prepare and characterize Sn-Bi nanoparticles," *Journal of Alloys and Compounds*. 2005, **394**, 282-285.

Crain, E.R.: Crain's Petrophysical Handbook. Web 17 November 2010. www.spec2000.net

Dey, A. and Morrison, H.F.: Resistivity Modeling for Arbitrarily Shaped Two-Dimensional Structures, Geophysical Prospecting 27, I06-I36, University of California, Berkeley, CA (1979).

Fukuda, D., Akatsuka, T., and Sarudate, M: "Characterization of inter-well connectivity using alcohol tracer and steam geochemistry in the Matsukawa vapor-dominated geothermal field, Northeast Japan," GRC Transactions. 2006, 797-801.

Gringarten, A.C. and Sauty, J. P.: "A theoretical study of heat extraction from aquifers with uniform regional flow," *Journal of Geophysical Research*. 1975, 4956-122.

Holder, D.S.: Electrical Impedance Tomography: Methods, History and Applications, IOP, UK (2004).

Horne, R.N.: "Reservoir Engineering of Reinjection," Course Notes. Stanford University, 1996.

Horne, R. N. and Szucs, P., Inferring Well-to-Well Connectivity Using Nonparametric Regression on Well Histories, *In Thirty-Second Workshop on Geothermal Reservoir Engineering, Stanford*, (2007) http://www.geothermal-energy.org/pdf/IGAstandard/SGW/2007/horne.pdf

Juliusson, E. and Horne, R. N., Characterization of Fractures in Geothermal Reservoirs, *In World Geothermal Congress. Bali*, (2010), http://www.geothermal-energy.org/pdf/IGAstandard/WGC/2010/2292.pdf

Kanj, M., Funk, J., and Al-Yousif, Z.: "Nanofluid Coreflood Experiments in the Arab-D," SPE paper 126161, presented at the 2009 SPE Saudi Arabia Technical Symposium and Exhibition held in Saudi Arabia, Alkhobar, May 09-11.

Kreft, A. and Zuber, A., On the physical meaning of the dispersion equation and its solutions for different initial and boundary conditions, *Chemical Engineering Science*, **33(11)**, (1978), p.1471–1480.

Lee, K. H., Ortega, A., Jafroodi, N., Ershaghi, I., A Multivariate Autoregressive Model for Characterizing Producer Producer Relationships in Waterfloods from Injection/Production Rate Fluctuations, *In SPE 2010 Western Regional Meeting, paper number SPE 132625*., (2010).

Levard, Clement. <clevard@stanford.edu (2010, July 8)>. [Personal email].

Lovekin, J. and Horne, R. N., Optimization of injection scheduling in geothermal fields, *In DOE Research and Development for the Geothermal Marketplace, Proceedings of the Geothermal Program Review VII,* (1989), pp. 45-52.

Matsunaga, I., Yanagisawa, N., Sugita, H., Tao, H.: "Reservoir monitoring by tracer testing during a long term circulation test at the Hijiori HDR site," *Proceedings*, Twenty-Seventh Workshop on Geothermal Reservoir Engineering, Stanford University. 2002.

Matsunaga, I., Yanagisawa, N., Sugita, H., Tao, H.: "Tracer tests for evaluation of flow in a multi-well and dual fracture system at the Hijiori HDR test site," *Proceedings*, World Geothermal Congress. 2005.

Maturgo, O.O., Sanchez, D. R., and Barroca, G.B.: "Tracer test using naphthalene disulfonates in Southern Negros Geothermal Production Field, Philippines," *Proceedings*, World Geothermal Congress. 2010.

Mufti, I.R.: Finite-Difference Resistivity Modeling for Arbitrarily Shaped Two-Dimensional Structures, *Geophysics*, **41**, (1976), 62-78.

Pritchett, J.W.: Finding Hidden Geothermal Resources in the Basin and Range Using Electrical Survey Techniques. A Computational Feasibility Study, report INEEL/EXT-04-02539 (2004).

Pruess, K. and Bodvarsson, G. S.: "Thermal effects of reinjection in geothermal reservoirs with major vertical fractures," *Journal of Petroleum Technology*. 1984, 1567-1578.

Sing, C., Kunzelman, J., and Weder, C.: "Time-temperature indicators for high temperature applications," *J. Mater. Chem.* **19** (2009).

Singha, K. and Gorelick, S.M. Saline Tracer Visualized with Three-dimensional Electrical Resistivity Tomography: Field-scale Spatial Moment Analysis. *Water Resources Research*, **41** (2005), W05023.

Slater, L., Binley, A.M., Daily, W. and Johnson, R. Cross-hole Electrical Imaging of a Controlled Saline Tracer Injection. *Journal of Applied Geophysics*, **44**, (2000), 85-102.

Spencer, R.L. and Ware, M.: Computational Physics 430, Partial Differential Equations, Department of Physics and Astronomy, Brigham Young University (2009).

Stacey, R.W., Li, K. and Horne, R.N.: Electrical Impedance Tomography (EIT) Method for Saturation Determination, *Proceedings*, 31st Workshop on Geothermal Reservoir Engineering, Stanford University, Stanford, CA (2006).

Tenma, N., Yamaguchi, T., and Zyvoloski, G.: Variation of the characteristics of the shallow reservoir at the Hijiori test site between 90-days circulation test and long-term circulation test using FEHM code." *Proceedings*, World Geothermal Congress. 2005.

The MathWorks: Partial Differential Equation Toolbox 1, The MathWorks™, Inc. (2003).

Villacorte, J. D., Malate, R. C. M. and Horne, R. N., Application of Nonparametric Regression on Well Histories of Geothermal Production Fields in the Philippines, *In World Geothermal Congress. Bali*, (2010), http://www.geothermal-energy.org/pdf/IGAstandard/WGC/2010/2311.pdf

Wang, P. and Horne, R.N.: Integrating Resistivity Data with Production Data for Improved Reservoir Modeling, SPE 59425, SPE Asia Pacific Conference, Yokohama, Japan (2000).

Wittung, P., Kajanus, J., Kubista, M., and Malmström, Bo G. (1994). "Absorption flattening in the optical spectra of liposome-entrapped substances," FEBS Letter 352, 37-40.